國 立 交 通 大 學
光 電 工 程 研 究 所

碩士論文

非極性"a"面氮化銦鎵多重量子井成長在奈米圖樣基板之光學特性研究

Optical properties of a-plane In$_{0.2}$Ga$_{0.8}$N/GaN multiple quantum wells grown on nanorod GaN templates

研究生：詹惟雯

指導教授：盧廷昌教授

郭浩中教授

中華民國九十九年七月

非極性"a"面氮化銦鎵多重量子井成長在奈米圖樣基板之光學特性研究

Optical properties of a-plane $In_{0.2}Ga_{0.8}N$/GaN multiple quantum wells grown on nanorod templates
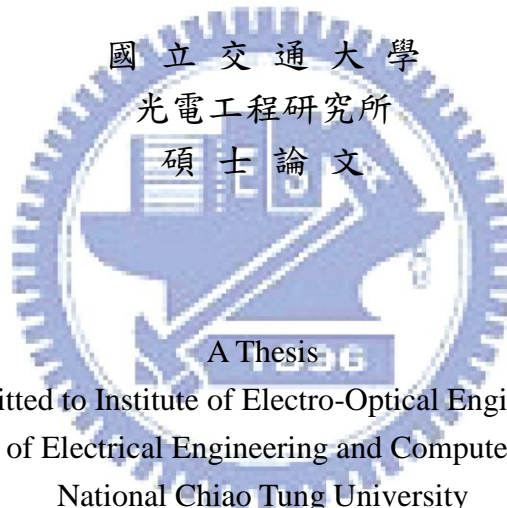
研究生:詹惟雯　　　　　　　　　Student: Wei. Wen. Chan

指導教授:盧廷昌 教授　　　　　　Advisor:Prof. Tien-Chang Lu

郭浩中 教授　　　　　　　　　Prof. Hao-Chung Kuo

國 立 交 通 大 學
光 電 工 程 研 究 所
碩 士 論 文

A Thesis
Submitted to Institute of Electro-Optical Engineering
College of Electrical Engineering and Computer Science
National Chiao Tung University
in Partial Fulfillment of the Requirements
for the Degree of
Master
In

Electro-Optical Engineering

June 2010
Hsinchu, Taiwan, Republic of China

非極性"a"面氮化銦鎵多重量子井成長在奈米圖樣基板之光學特性研究

研究生:詹惟雯　　　　　　　　　　　指導教授:盧廷昌 教授

郭浩中 教授

交通大學光電工程研究所

摘要

在本論文中，我們利用有機金屬化學氣相沉積法成長非極性"a"平面氮化銦鎵/氮化鎵多重量子井的結構，樣品的差異為氮化鎵基板中不同的奈米柱(Nanorod)深度。在特性分析中，包含了光學與結構特性上的相關研究；在發光特性方面，所利用的是光激發螢光光譜(PL)進行樣品的光學特性分析，結構及相關成分的研究包含了掃描式和穿透式電子顯微鏡圖像、原子力顯微鏡、X射線繞射…。

由AFM、TEM可知，奈米柱深度越深再成長的氮化鎵基板，表面的質地越好，藉由變溫PL的量測，可以得到室低溫強度比隨著奈米柱深度越深值越大，活化能也提升，意味著減少樣板的缺陷，多重量子井的侷限能力會提升；在變功率的PL實驗中，樣品的發光波長不隨著雷射功率增加而改變，得知非極性面成長的氮化銦鎵多重量子井能確實抑制QCSE的效應。在非極性結構的極化發光特性量測中，我們發現發光極化率、能量差會隨著奈米柱深度越深而降低，顯示了應力的改變，再經由模擬得到驗證。

接著，我們量測變溫變功率 PL 的內部量子效率，得到經由奈米柱深度 1.7 微米（最深）成長的樣品是 39％，而直接成長的樣品是 13％，再透過實驗數據的分析，得到非輻射係數（A），隨著奈米柱深度越深而降低，與 TEM 估算出來的錯位密度缺限變化相吻合，所以在奈米柱深度 1.7 微米有最佳的載子捕捉及放光效率。

Optical properties of a-plane In$_{0.2}$Ga$_{0.8}$N/GaN multiple quantum wells grown on nanorod GaN templates

Student: Wei Wen Chan   Advisors: Prof. Tien-Chang Lu

Prof. Hao-Chung Kuo

Institute of Electro-Optical Engineering, National Chiao Tung University

Abstract

In this thesis, we investigated a-plane InGaN/GaN multiple quantum wells were grown on r-plane sapphire by metal organic chemical vapor deposition, and the difference of samples is nanorod depth of *a*-plane GaN templates. We utilized several methods including photoluminescence（PL）, atomic force microscopy（AFM）, and transmission electron microscopy（TEM）to investigate the optical characteristics and material structures of our samples.

We have known that the crystal quality of *a*-plane GaN films was improved by using epitaxial lateral overgrowth on a nanorod GaN template by AFM and TEM. And from the temperature dependent PL measurement, we get the result which the value of IQE$_{PL}$ and activation energy is higher when the etching depth of nanorods is deeper. It means carries confinement in MQWs was enhanced by lowering defects of *a*-plane GaN templates. Moreover, the un-shift emission peak from the power-dependent PL measurement indicated the absence of QCSE within our samples. The polarization-dependent PL shows that the degree of polarization and peak energy shift decreased with increasing nanorods depth, which can be attributed to stain relaxed ,

injection carrier density and scattering.

In the second part, we measure the internal quantum efficiency（IQE）of the MQWs, and the IQE of a-plane InGaN/GaN MQWs are approximately 39%(1.7um) more than 13%(as-grown). Next, using the measured data and knowing the *B* value, one can obtain nonradiative coefficient *A*. The measured nonradiative recombination coefficient A decreased one order as the etching depth increases from 0 to 1.7 um. It matched the variation of threading dislocation density and we could observe the best luminescence efficiency and quality with 1.7um nanorod sample.
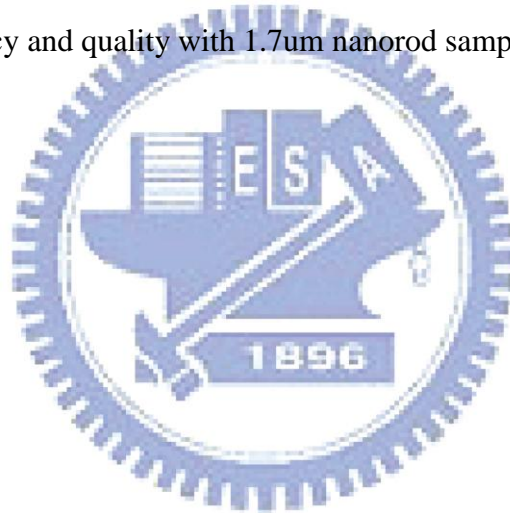
致謝

時光飛逝，沒想到馬上就輪到我畢業了，回頭想想這兩年實驗室的點點滴滴，其實也蠻令人感傷的，首先一定要先感謝我們的三位老師：王老師、盧老師和郭老師，相信未來三位老師們一定能帶領實驗室為台灣做出更好的研究成果。

可以順利的完成研究內容，最感謝的就是碩均學長，提供我一系列的樣品，以及指導我如分析數據，一起討論下一步該怎麼做，不會無謂的浪費時間，有效地解決問題；另外也非常感謝輝閎學長、俊榮學長、清華學長和卓木學長，在研究上都對我有非常大的幫助。在碩士的兩年生活裡，與我生活關係最密切的就是一起同甘共苦的同學們，謝謝依寧、婉君，從大學一起到研究所，我們總是有聊不完的話題，感覺妳們常常要聽我發牢騷，是我研究所最好的伴；也謝謝永吉、大為等碩二的同學，大家常常一起吃飯、聊天、玩樂、修課，讓我的碩士生活更多采多姿。

最後謝謝我的家人，感謝我的爸爸媽媽的支持，讓我順利完成學業，謝謝你們。

Content

Chapter 1 Introduction and Motivation

Chapter 2 Properties of nonpolar multiple quantum wells (MQWs) structure

Chapter 3 Sample growth and experimental instrument

Chapter 4 Optical properties of *a*-plane In$_{0.2}$Ga$_{0.8}$N/GaN multiple quantum wells with nanorod templates

Chapter 5 Characteristics of emission polarization in *a*-plane nanorods embedded with InGaN/GaN MQWs

Chapter 6 Conclusion and future work

List of Tables

List of Figures

Chapter 1 Introduction and Motivation

1.1 The development of Ⅲ-Nitride nanostructure from c-plane to a-plane

In the past, GaN-based semiconductor had attracted much attention for commercial applications in developing high quality optoelectronic devices. A number of studies have reported laser diodes and light emitting diodes grown on sapphire、6H-SiC、or free-standing GaN along c-plane [0001] crystal orientation. However, the optoelectronic device grow along [0001] axis that the built-in electric field may exist in the nanostructure. The built-in electric field consists of spontaneous polarization and piezoelectric polarization. The built-in electric field would result in potential bending which called quantum confined stark effect (QCSE) [1, 2]. This would result in decreasing the oscillation strength of the separation of electron-hole pairs. Also, the carrier recombination rate and the internal quantum efficiency (Fig. 1.1.1) would be reduced. In order to improve the internal quantum efficiency, the issue related to overcome the built-in electric field within the multiple quantum wells (MQWs) is very important.

Recently, several groups have grown samples on the nonpolar structures to eliminate the built-in electric field. There are two approaches of nonpolar structures in common. One is growing [1010] m-plane heterostructures on γ-LiAlO$_2$(100) by hydride vapor phase epitaxy (HVPE) and molecular beam epitaxy (MBE) [3,4]. The

other one is growing [1120] *a*-plane heterostructures on *r*-plane sapphire or *a*-plane SiC

by metalorganic vapor-phase (MOVPE) [5-7]. The planes with different orientations of

hexagonal wurtize structure of GaN are showed in Fig. 1.1.2. Nowadays, nonpolar

structure has been used to grow AlGaN/GaN and InGaN/GaN heterostructures.

The optical characteristics of *c*-plane heterostructures have been investigated

intensively [8-9]. However, the optical properties of nonpolar heterostructures have

been still worth studying. In these few years, many groups have made efforts on the

structure growth condition and the light efficiency improvement such as nonpolar and

nanorod structures [5, 10-12]. In this thesis, we will discuss the optical properties and

the carrier recombination mechanisms of nonpolar *a*-plane InGaN/GaN MQWs.

1.2 The characteristics of a-plane GaN films

Recent studies of InGaN/GaN multiple quantum wells demonstrate that it is

possible to eliminate such polarization fields along the nonpolar orientation. However,

the difficulty to utilize nonpolar GaN is not a suitable substrate for heteroepitaxial

a-plane GaN growth. In general, the threading dislocation (TD) density of $\sim 3 \times 10^{10}$

cm^{-2} and a basal stacking fault density of $\sim 3.5 \times 10^{5}$ cm^{-1} were commonly observed in

a-plane GaN grown on *r*-plane sapphire. The TDs in GaN act as nonradiative

recombination centers which are responsible for poor internal quantum efficiency

(IQE). Therefore, the reduction in TD density is essential to improve the *a*-plane

device performance. Lateral epitaxial overgrowth (LEO) techniques have been employed to achieve defect reduction in nonpolar GaN. Previous LEO methods include SiNx nanomask LEO [13], single-step LEO [14], selective area LEO (SALE) [15], sidewall LEO, [16] and so on.

However, the regrowth thickness of these LEO techniques is usually larger than 20 um to achieve a better coalescence surface, causing the difficulty in layer uniformity control. In this thesis, we propose an approach of lateral overgrowth on nanorod *a*-plane GaN template to realize the defect reduction and quality improvement in the subsequently grown *a*-plane GaN layer. Compared with the above-mentioned LEO techniques, the nanorod epitaxial lateral overgrowth (NRELOG) is highly advantageous for thinner.

1.3 Fabrication of nanostructure materials

Low dimension structure as the active layer was widely applied in these optical devices to operate in low threshold current, reduce temperature sensitivity and enhance the emitting efficiency due to quantum confine effect [4-5]. Because of the different dimensional confinement of carrier and density of state, the nanostructure can be classify into quantum well (QW), nanowire and quantum dot (QD) by their density of state as shown in Fig. 1.3.1. The bulk material has three dimensional density of state and the shape is parabolic function, the energy state of carrier is

continues above energy band-gap. Then two dimensional structures, such as quantum well, is a step function due to one dimensional confinement of carrier. With decreasing the degree of freedom of carriers, the density of state of zero-dimensional structure, as quantum dot, manifest delta function density of state. As a result, the electronic states are quantized and the energy levels become discrete. In Figure 1.3.2, we could see the carriers are localized in the quantum dot structure of three dimensional confinements. There are some unique characteristics in the quantum dot structures. Discrete energy state is an attractive benefit applied to decrease the half of full width in emitting spectrum and separate the different quantum state level. The lasing behavior and quantum information analysis can be improved by their development.
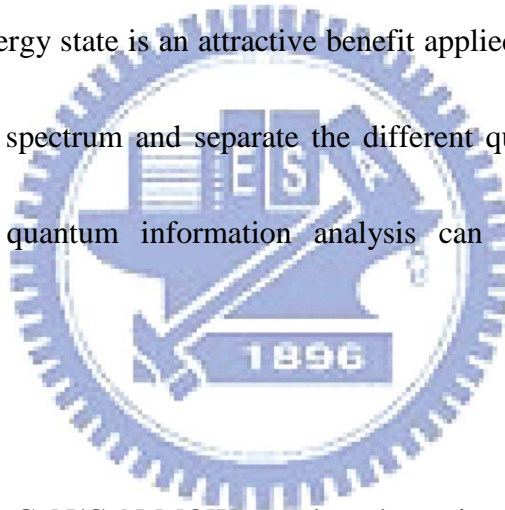
1.4 Motivation

Conventionally, InGaN/GaN MQWs used as the active layers of UV to visible light-emitting diodes (LEDs) and laser diodes (LDs) were grown along [0001] *c*-axis. Due to the existence of spontaneous and piezoelectric polarization fields, spatial separation of the electron and hole wave functions in conventional *c*-plane nitride-based quantum wells restrict the carrier recombination efficiency. To avoid such polarization effects, growth along the [11-20]-oriented direction has been explored for planar *a*-plane GaN on *r*-plane sapphire. Up to now, however, the

structural and optical properties of nonpolar InGaN/GaN MQWs are still inferior compared to their mature *c*-plane grown counterpart due to much higher dislocation densities when grown on *r*-plane sapphire substrates.

In this thesis, we propose an approach of lateral overgrowth on nanorod *a*-plane GaN template to realize the defect reduction and quality improvement in the subsequently grown *a*-plane GaN layer [17]. Moreover, the crystal quality of a-plane GaN films would vary with the etching depth of nanorod because the etching depth could affect contact area with sapphire. The TDs in GaN act as nonradiative recombination centers which are responsible for poor internal quantum efficiency (IQE).We want to know the relationship between optical properties of MQWs and the crystal quality of nanorod GaN template. We investigated the optical characteristics and internal quantum efficiency of nonpolar *a*-plane InGaN/GaN MQWs with different etching depth of nanorod. A series of optical measurements and material analysis were performed to further acquaint ourselves with a- plane InGaN/GaN MQWs.

The organization of this thesis is as following: In chapter 2, we discuss the characteristics of GaN-based nanostructures. The experimental principle and set up are described in chapter 3. In chapter 4, we study the optical properties of *a*-plane InGaN/GaN MQWs with different nanorod GaN template. We present the experimental results of *a*-plane nanorods with embedded InGaN/GaN MQWs

compared with the behavior of as-grown MQWs in chapter 5. Finally, we give a brief

conclusion of the thesis in chapter 6.
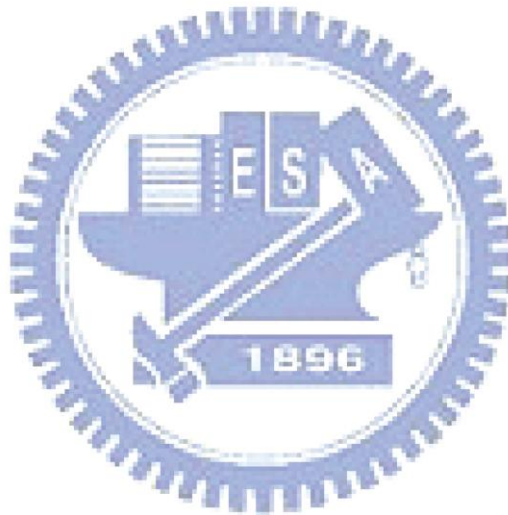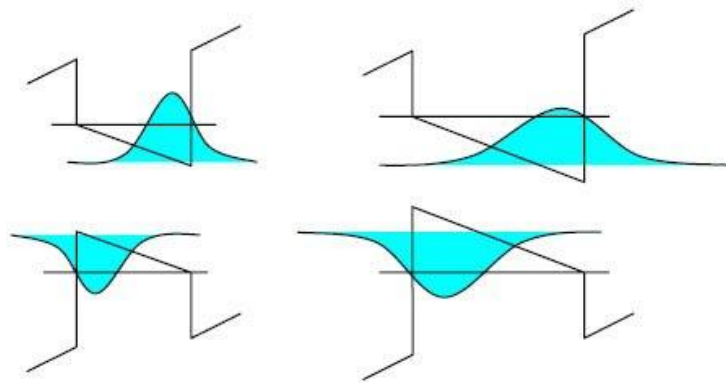
Fig. 1.1.1 Band bending resulted from QCSE in polar quantum well with different thicknesses
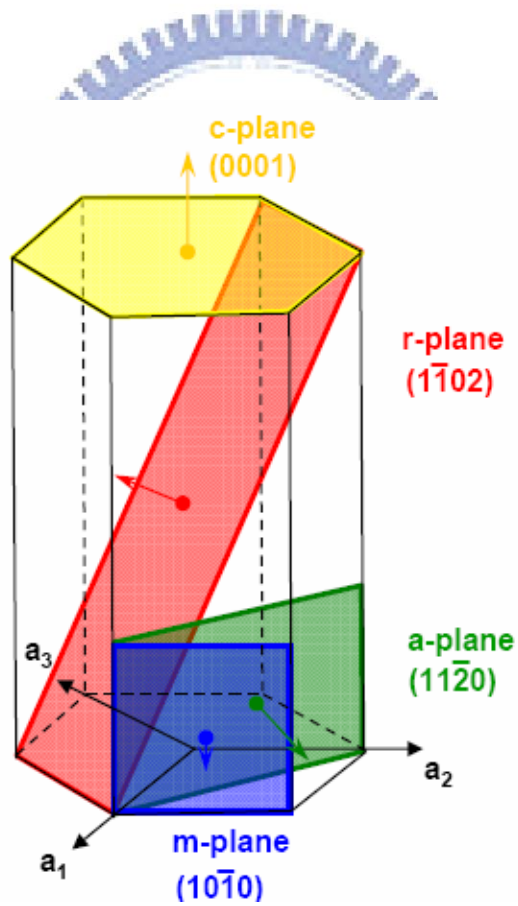
Fig. 1.1.2 The planar relation and orientation in hexagonal crystal structure
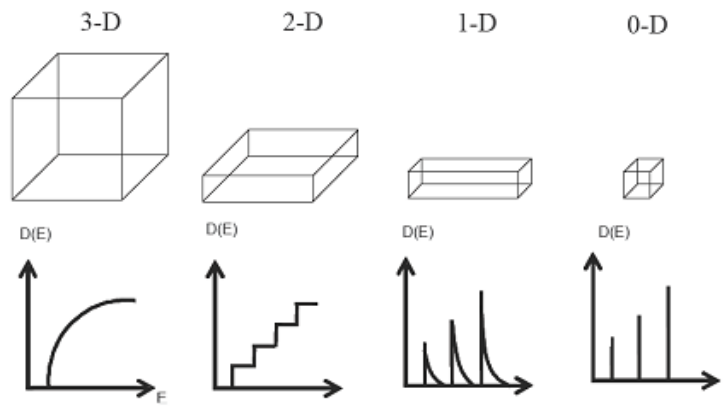
Fig 1.3.1 Dimension of nanostructure and corresponding density of state
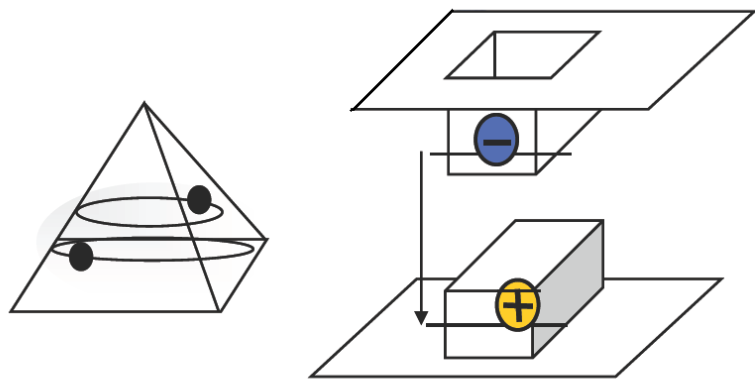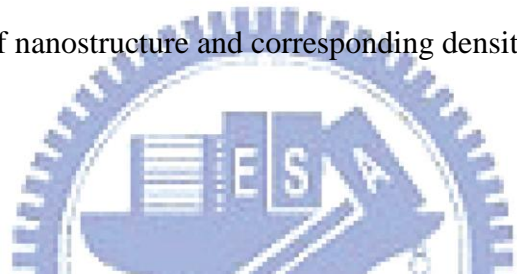
Fig. 1.3.2 The carrier behavior in three dimensional confinement structure

Chapter 2 Properties of nonpolar multiple quantum wells (MQWs) structure

2.1 Quantum confinement effect in semiconductor nanostructure

The semiconductor nanostructure is widely used as the active layer in optoelectric devices such as light emitting diodes and laser diodes. If we make very small crystals, the optical properties of solids will depend on their size. The size dependence of the optical properties in very small crystals is a consequence of the quantum confinement effect. What "Quantum confinement" means is that when electrons and holes in a semiconductor are restricted in one or two or even three dimensions. For example, a quantum dot is confined in all three dimensions, a quantum wire is confined in two dimensions, and a quantum well is confined in one dimension. Therefore, quantum confinement occurs when one or more of the dimensions of a nanostructure are very small so that it approaches the size of an exciton in bulk crystal, called the Bohr exciton radius. [18] In this thesis, we talk about quantum well structure which is a structure where the height is approximately the Bohr exciton radius while the length and breadth in the other two dimensions are relatively free from constraint.

The distance between the electron and the hole is called the effective Bohr radius, a_B of the exciton. When the well width is much larger than a_B in bulk, the exciton binding energy will not show evident difference between the well and the bulk, for the

excitons feel nearly the same environment as in bulk. As the well width is decreased

to the order or less than the order of a_B, the wave functions of electrons and holes

overlap get improved and are confined in the well. This also improves the exciton

binding energy.

The Hamiltonian describing the relative motion of the exciton could be written as

$H=H_e(x_e) +H_h(x_h) +H_{e-h}(r)$

where H_e and H_h are the Hamiltonian describing the electron and hole motion

confined in the well. H_{e-h} is the Hamiltonian includes the kinetic energy part of the

relative motion of the exciton in the Y-Z plane and the Coulomb potential attracting

the electron and the hole in the three dimensional form. The x-coordinate of the

electron and hole is denoted as x_e and x_h while r represent the relative position vector

between the electron and the hole. Therefore the eigenvalue solved is given by

$E_n= E^e_{xn} +E^h_{xn}-E_{e-h}$

where E^e_{xn} and E^h_{xn} is the energy of nth quantum confined state, and E_{e-h} is the

binding energy of exciton defined as positive value. Therefore, the lowest exciton

resonance energy associated with the ground state in the quantum well could be

written as $E_{emission} = E_g+ E^e_{xn} +E^h_{xn}-E_{e-h}$

The resonance energy was sensitive to well width and the monatomic well size

fluctuation in the narrower well. The well width dependence of the absorption spectra

is determined by competition between the quantum confinement energy level and the

exciton binding energy.

2.2 The localization effect in quantum well structure

As we mentioned in chapter 1, there existed built-in electric field in conventional

c-plane heterostructures. This would result in decreasing the oscillation strength of the

separation of electron-hole pairs. Also, the carrier recombination rate and the internal

quantum efficiency would be reduced. However, in spite of the high density of

dislocations and large separation of electron-hole pairs, the InGaN-based

heterostructures grown on c-plane sapphire still have the high luminescence efficiency.

It is reported that the luminescence efficiency enhancement is due to the effective

localization of excitons in the In-rich regions [19]. The mechanism of this unique

behavior in InGaN-based heterostructures is still unclear. Several groups suggested that

the localization of excitons might induce by the composition fluctuation and the phase

separation [20,21].

In the In-rich regions, it would provide a deep potential minimum within the

InGaN layers, which would confine electrons and holes tightly. Once the carriers

injected into the InGaN-based heterostructures, they will not be captured by the defects

or dislocations. The effectively trapping of carriers improved the radiative

recombination rate. Otherwise, the exciton localization is influenced by quantum well

thickness, In content, and doping level. The increase of In content may increase the

effective localization depth but also induce more nonradiative defect densities [22].

2.3 The basic concept of nonpolar nanostructure

In conventional polar *c*-plane heterostructures, there exist two kinds of built-in

electronic field: spontaneous polarization and piezoelectric polarization. The

spontaneous polarization is due to the difference of the lattice parameters from the ideal

values, so it would induce molecular dipoles in the material creating a polarization field.

The piezoelectric field occurs due to the difference of thermal expansion coefficient,

which causes compressive/tensile strain between the multilayers.

InGaN/GaN multiple quantum wells are a widely used material and structure to

serve as the active layer in nitride heterostructures for its advantage in easy tuning

wavelength through controlling the composition of indium. However conventional

InGaN/GaN quantum wells grown along the crystallographic c-axis exhibit an internal

spontaneous and piezoelectric field in the MV/cm range. The spontaneous field is

induced from different atoms arrange in one direction parallel with the growth axis

while the piezoelectric field is caused by biaxial compressive strain due to the lattice

mismatch between InGaN and GaN.

The built-in electric field would result in potential bending which called quantum

confined stark effect (QCSE). In order to overcome QCSE, the nonpolar structure has

been developed. In the nonpolar structure, the Ga and N growth direction is normal to

the growth axis, so there is not built-in electric field along the growth axis. Therefore,

the separation of the electron and hole wavefunction is decreased and the radiative

recombination rate is also improved in this flat-band structure. The polar and nonpolar

band diagrams are illustrated in Fig. 2.3.1.

The nonpolar structure is important not only because of its flat-band structure

without the built-in electric field but also the polarization anisotropic property used in

optoelectric devices. In recent years, several groups have investigate nonpolar [1010]

m-plane GaN films [21] and heterostructure [3,4] on γ -LiAlO$_2$(100) by hydride vapor

phase epitaxy (HVPE) and molecular beam epitaxy (MBE) as well as [1120] *a*-plane

GaN films [23] and heterostructures [5-7] on *r*-plane sapphire or *a*-plane SiC by

metalorganic vapor-phase (MOVPE). However, the optical properties of nonpolar

heterostructures have still been unclear and worth studying.
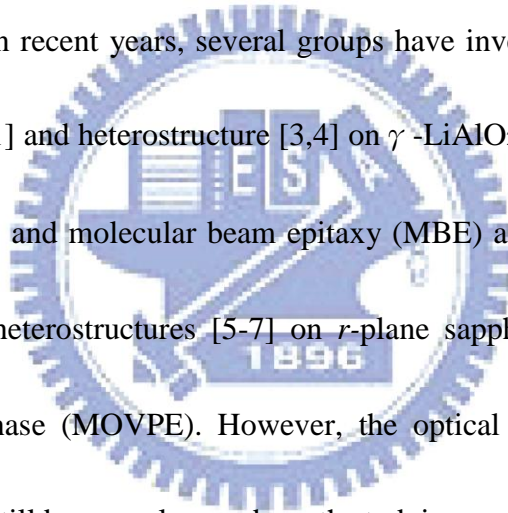
2.4 In-plane light polarization effect in nonpolar nanostructure

Nonpolar structures are different from polar *c*-plane structures, which do not

suffer from QCSE and also have the advantage of the in-plane anisotropic optical

properties. This polarization anisotropic property is desirable in several applications

such as back-lighting in liquid crystal display since conventional polarizers would not

be required.

In conventional GaN films grown on *c*-plane substrate, the strain in x-y plane of WZ-GaN is isotropic symmetry (with strain$\varepsilon_{xx} = \varepsilon_{yy}$). However, it would have anisotropic biaxial strain when GaN films grown on nonpolar *a*-plane or *m*-plane substrates. This could be explained that the *c*-axis lies within the film planes. The in-plane polarization anisotropic properties have already observed in GaN films [21] and GaN/AlGaN multiple quantum wells [25].

The valence bands of WZ-GaN in the order of decreasing electron energy are heavy-hole (HH), light-hole (LH), and crystal field split-off hole (CH). The coordinate system used here for studied is x//*a* [11-20] , y//*m* [1-100] , and z//*c* [0001] as shown in Fig. 2.4.1. Because WZ-GaN has in-plane symmetry in x-y plane, the wave functions of HH and LH could be represented as $|X+iY\rangle$ and the wavefuction of CH could be referred to $|Z\rangle$. In the case of nonpolar structures, for example *m*-plane GaN films, there would be anisotropic biaxial strain within the in-plane (x-z plane). Therefore, the anisotropic strain would break the symmetry in x-y plane and the wavefunctions $|X+iY\rangle$ would be separated into $|X\rangle$ and $|Y\rangle$. The compressive strain along x direction would induce a dilation along y direction so it rearranged the order of valence bands into $|X\rangle$-like, $|Z\rangle$-like and $|Y\rangle$-like states. Under this situation, the lowest transition is totally linearly polarized along x-direction (E//C) and the second lowest transition is totally polarized along z-direction (E⊥C). The third lowest transition is

totally polarized along y-direction (E//C).

A significant two emission peaks of different energy has been observed due to the valence band rearrangement [26]. However, there are some reports indicated that there is not any spectral shift can be observed in the PL measurement [24, 27]. This result can be explained as mixing of valence band states or the presence of localization states [21, 27].

2.5 The formation of nanorods structure

Due to the rapid development of fabrication methods for nanostructures, various nano-structure fabrication methods have been developed. For GaN-based materials, the fabrications and synthesizing of GaN nanowires and nanorods have been investigated using several methods such as carbon nanotube confined reaction, metal-catalyzed growth assisted by laser ablation, and the high temperature pyrolysis approach etc. However, all these reported methods had not mentioned about the control of dimension and density of their nanostructure. Our groups have reported a novel technique to fabricate GaN-based nanorod templates with controllable dimension and density using self-assemble nickel nano-mask and inductively coupled plasma reactive ion etching (ICP-RIE) [17]. The experimental process of nanorod epitaxial lateral overgrowth (NRELOG) is shown in chapter 4.
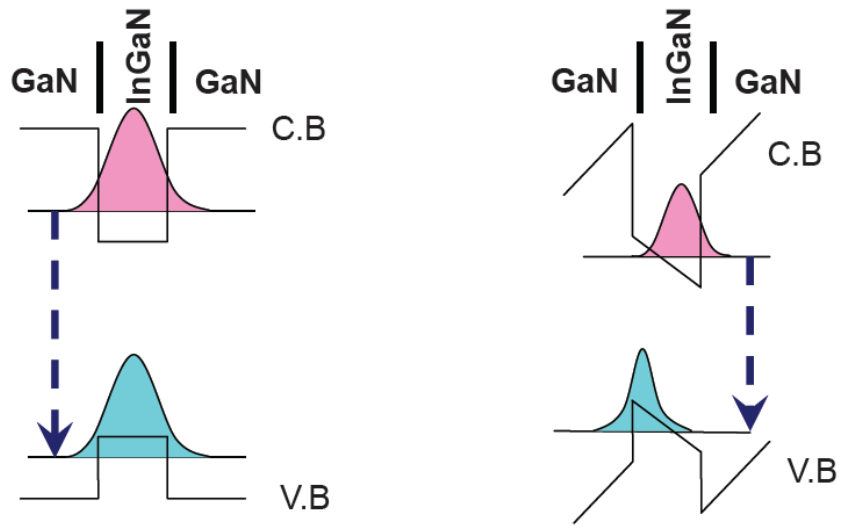
Fig. 2.3.1 The band diagrams of (a) nonpolar quantum wells and (b) polar quantum

wells
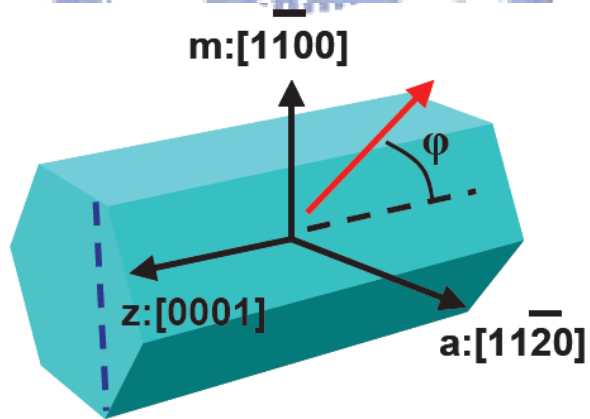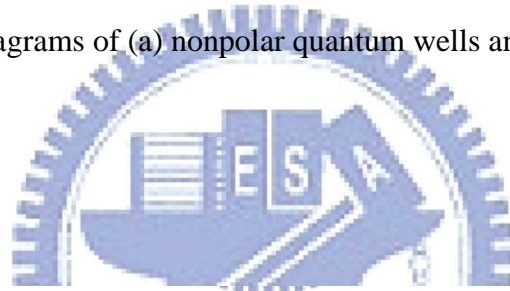
Fig. 2.4.1 The definition of the coordinate system for our samples

Chapter 3 Sample growth and experimental instrument

3.1 Growth mechanism of InGaN/GaN MQWs using metal organic chemical vapor deposition (MOCVD)

Metal organic chemical vapor deposition (MOCVD) is a chemical vapour deposition method of epitaxial growth of materials, especially compound semiconductors from the surface reaction of organic compounds or metalorganics and metal hydrides containing the required chemical elements. For example, indium phosphide could be grown in a reactor on a substrate by introducing Trimethylindium $((CH_3)_3In)$ and phosphine (PH_3). Alternative names for this process include organometallic vapour phase epitaxy (OMVPE), metalorganic chemical vapour deposition (MOCVD) and organometallic chemical vapour deposition (OMCVD). Formation of the epitaxial layer occurs by final pyrolysis of the constituent chemicals at the substrate surface. In contrast to molecular beam epitaxy (MBE) the growth of crystals is by chemical reaction and not physical deposition. This takes place not in a vacuum, but from the gas phase at moderate pressures (2 to 100 kPa). As such this technique is preferred for the formation of devices incorporating thermodynamically metastable alloys. It has become the dominant process for the manufacture of laser diodes, solar cells, and LEDs.
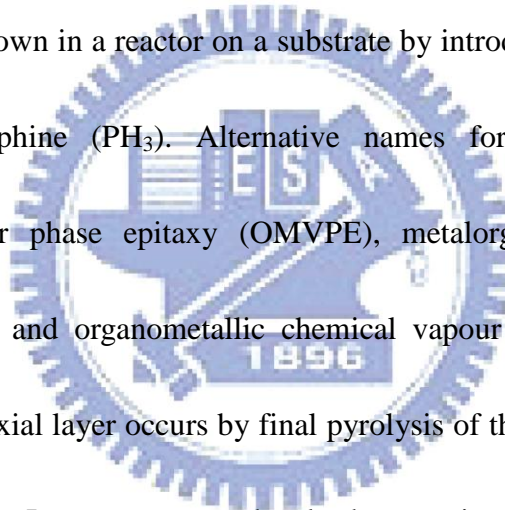
A reactor is a chamber made of a material that does not react with the chemicals being used. It must also withstand high temperatures. This chamber is composed by reactor walls, liner, a susceptor, gas injection units, and temperature control units. Usually, the reactor walls are made from stainless steel or quartz. To prevent over heating, cooling water must be flowing through the channels within the reactor walls. Ceramic or special glasses, such as quartz, are often used as the liner in the reactor chamber between the reactor wall and the susceptor. A substrate sits on a *susceptor* which is at a controlled temperature. The susceptor is made from a material resistant to the metalorganic compounds used; graphite is sometimes used. For growing nitrides and related materials, a special coating on the graphite susceptor is necessary to prevent corrosion by ammonia (NH_3) gas. (Fig3.1.1)
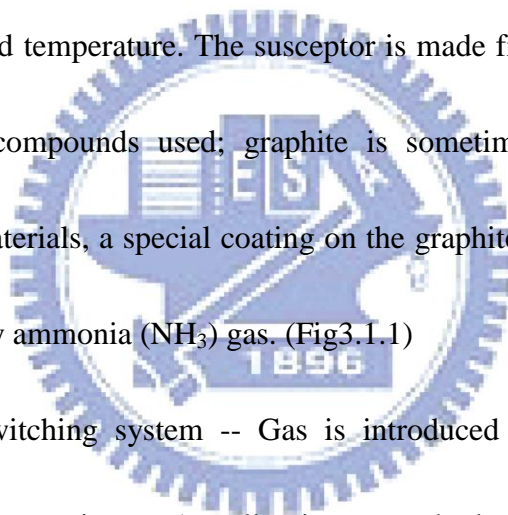
Gas inlet and switching system -- Gas is introduced via devices known as 'bubblers'. In a bubbler a carrier gas (usually nitrogen or hydrogen) is bubbled through the metalorganic liquid, which picks up some metalorganic vapour and transports it to the reactor. The amount of metalorganic vapour transported depends on the rate of carrier gas flow and the bubbler temperature, and is usually controlled automatically and most accurately by using a Piezocon type vapour control system. Allowance must be made for saturated vapours.

Pressure maintenance system.

Gas Exhaust and cleaning System -- Toxic waste products must be converted to liquid or solid wastes for recycling (preferably) or disposal. Ideally processes will be designed to minimize the production of waste products.

3.2 Transmission Electron Microscope (TEM), Atomic Force Microscopy（AFM）and Scanning electron microscope (SEM)

1. Transmission Electron Microscope (TEM)

Transmission electron microscope is the pre-eminent method for determining dislocation' and other crystallographic defects character and for performing chemical and crystallographic analysis of micrometer and smaller precipitates and other microstructures. With the similar structure and more powerful function compared with SEM, TEM offers the in-depth perspective of specimen characterizations.
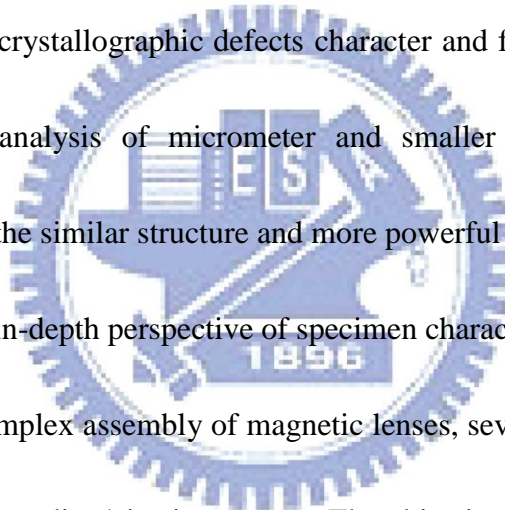
Any TEM is a complex assembly of magnetic lenses, several apertures, a sample holder and an image recording/viewing system. The objective lens forms a diffraction pattern in the back focal plane with electrons scattered by the sample and gombines them to generate an image in the image plane (1. intermediate image). Thus, diffraction pattern and image are simultaneously present in the TEM. It depends on the intermediate lens which of them appears in the plane of the second intermediate image and magnified by the projective lens on the viewing screen. Switching from real space (image) to reciprocal space (diffraction pattern) is easily achieved by

changing the strength of the intermediate lens. In imaging mode, and objective

aperture can be inserted in the back focal plane to select one or more beams that

contribute to the final image (BF, DF, HRTEM). In selected area electron diffraction

(SAED), an aperture in the plane of the first intermediate image defines the region of

which the diffraction is obtained.

In the bright field (BF) mode of the TEM, an objective aperture is placed in the

back focal plane of the objective lens which allows only the direct beam to pass. In

this case, mass-thickness and diffraction contrast contribute to image formation: thick

areas, areas in which heavy atoms are enriched, and crystalline areas appear with dark

contrast. In spite of the useful information obtainable from BF images, it should be

mentioned that the interpretation of contrast is often impeded since these phenomena

occur simultaneously.
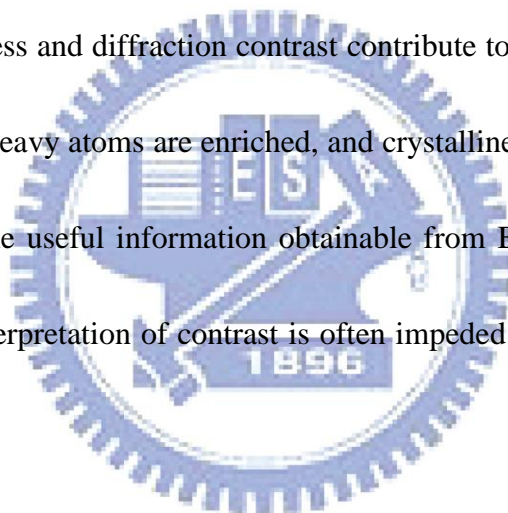
In dark field (DF) images, one or more diffracted beams are allowed to pass the

objective aperture. The direct beam is blocked by the aperture. In contrast to the direct

beam, the diffracted beam has interacted strongly with the specimen, and often very

useful information is present in DF images, e.g., about planar defects, stacking faults

or particle size.

To obtain lattice images, a larger objective aperture has to be selected that allows

many beams including the direct beam to pass. The image is formed by the

interference of the diffracted beams with the direct beam (phase contrast). If the point

resolution of the microscope is sufficiently high and a suitable sample oriented along

a zone axis, then high-resolution TEM (HRTEM) images are obtained. In many cases,

the atomic structure of the specimen can directly be investigated by HRTEM.

The incident parallel electron wave interacts elastically while passing through the

specimen, and the resulting modulations of its phase and amplitude are present in the

electron wave leaving the specimen. The wave here, the object exit wave o(r), thus

contains the information about the object structure. The objective lens performs 1.

The Fourier Transform (Fourier analysis) that creates the diffraction pattern of the

object in the back focal plane and 2. the inverse Fourier Transform (Fourier synthesis)

that makes the interference of the diffracted beams back to a real space image in the

image plane (lattice image).
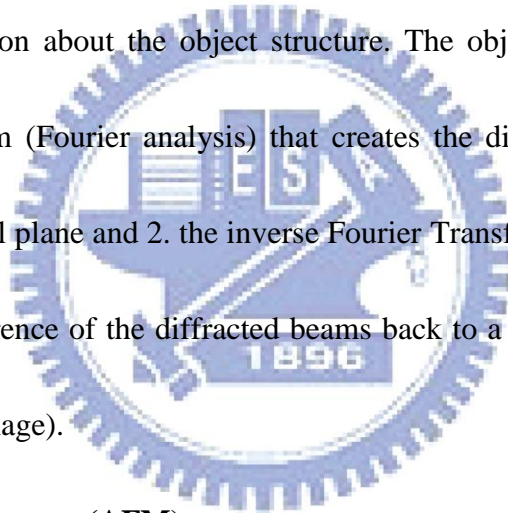
2. Atomic force microscopy (AFM)

Atomic force microscopy (AFM) or scanning force microscopy (SFM) is a very

high-resolution type of scanning probe microscopy, with demonstrated resolution of

fractions of a nanometer, more than 1000 times better than the optical diffraction limit.

The precursor to the AFM, the scanning tunneling microscope, was developed by

Gerd Binnig and Heinrich Rohrer in the early 1980s at IBM Research - Zurich, a

development that earned them the Nobel Prize for Physics in 1986. Binnig, Quate and

Gerber invented the first atomic force microscope (also abbreviated as AFM) in 1986. The first commercially available atomic force microscope was introduced in 1989. The AFM is one of the foremost tools for imaging, measuring, and manipulating matter at the nanoscale. The information is gathered by "feeling" the surface with a mechanical probe. Piezoelectric elements that facilitate tiny but accurate and precise movements on (electronic) command enable the very precise scanning. In some variations, electric potentials can also be scanned using conducting cantilevers. In newer more advanced versions, currents can even be passed through the tip to probe the electrical conductivity or transport of the underlying surface, but this is much more challenging with very few groups reporting reliable data.
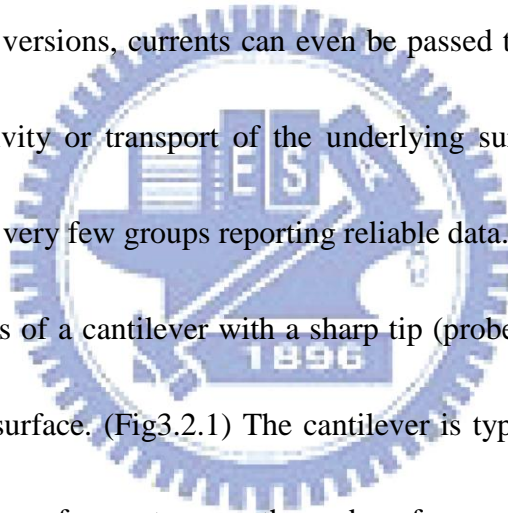
The AFM consists of a cantilever with a sharp tip (probe) at its end that is used to scan the specimen surface. (Fig3.2.1) The cantilever is typically silicon or silicon nitride with a tip radius of curvature on the order of nanometers. When the tip is brought into proximity of a sample surface, forces between the tip and the sample lead to a deflection of the cantilever according to Hooke's law. Depending on the situation, forces that are measured in AFM include mechanical contact force, van der Waals forces, capillary forces, chemical bonding, electrostatic forces, magnetic forces (see magnetic force microscope, MFM), Casimir forces, solvation forces, etc. As well as force, additional quantities may simultaneously be measured through the use of

specialized types of probe (see scanning thermal microscopy, photothermal microspectroscopy, etc.). Typically, the deflection is measured using a laser spot reflected from the top surface of the cantilever into an array of photodiodes. Other methods that are used include optical interferometry, capacitive sensing or piezoresistive AFM cantilevers. These cantilevers are fabricated with piezoresistive elements that act as a strain gauge. Using a Wheatstone bridge, strain in the AFM cantilever due to deflection can be measured, but this method is not as sensitive as laser deflection or interferometry.

If the tip was scanned at a constant height, a risk would exist that the tip collides with the surface, causing damage. Hence, in most cases a feedback mechanism is employed to adjust the tip-to-sample distance to maintain a constant force between the tip and the sample. Traditionally, the sample is mounted on a piezoelectric tube, that can move the sample in the *z* direction for maintaining a constant force, and the *x* and *y* directions for scanning the sample. Alternatively a 'tripod' configuration of three piezo crystals may be employed, with each responsible for scanning in the x,y and z directions. This eliminates some of the distortion effects seen with a tube scanner. In newer designs, the tip is mounted on a vertical piezo scanner while the sample is being scanned in X and Y using another piezo block. The resulting map of the area *s* = *f(x,y)* represents the topography of the sample.
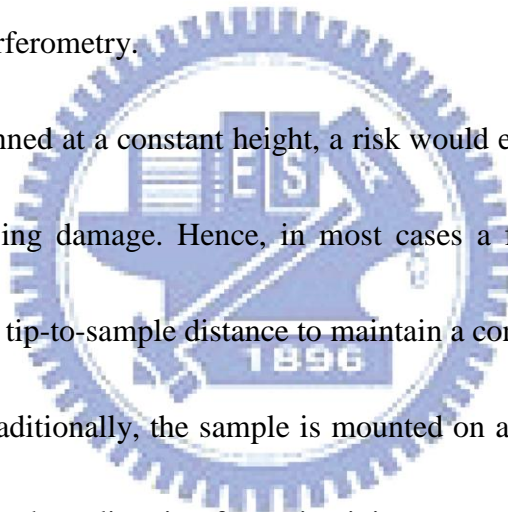
The AFM can be operated in a number of modes, depending on the application. In general, possible imaging modes are divided into static (also called *contact*) modes and a variety of dynamic (or non-contact) modes where the cantilever is vibrated.

3. Scanning electron microscope (SEM)

The scanning electron microscope (SEM) is a type of electron microscope that images the sample surface by scanning it with a high-energy beam of electrons in a raster scan pattern. (Fig. 3.2.3)The electrons interact with the atoms that make up the sample producing signals that contain information about the sample's surface topography, composition and other properties such as electrical conductivity.

The types of signals produced by an SEM include secondary electrons, back-scattered electrons (BSE), characteristic X-rays, light (cathodoluminescence), specimen current and transmitted electrons. Secondary electron detectors are common in all SEMs, but it is rare that a single machine would have detectors for all possible signals. The signals result from interactions of the electron beam with atoms at or near the surface of the sample. In the most common or standard detection mode, secondary electron imaging or SEI, the SEM can produce very high-resolution images of a sample surface, revealing details about less than 1 to 5 nm in size. Due to the very narrow electron beam, SEM micrographs have a large depth of field yielding a characteristic three-dimensional appearance useful for understanding the surface
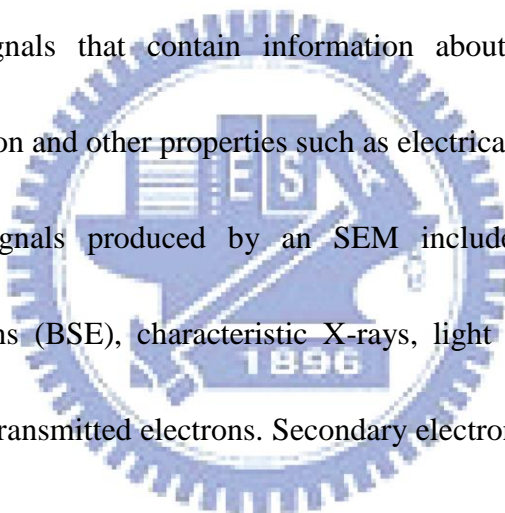
structure of a sample. This is exemplified by the micrograph of pollen shown to the

right. A wide range of magnifications is possible, from about 10 times (about

equivalent to that of a powerful hand-lens) to more than 500,000 times, about 250

times the magnification limit of the best light microscopes. Back-scattered electrons

(BSE) are beam electrons that are reflected from the sample by elastic scattering. BSE

are often used in analytical SEM along with the spectra made from the characteristic

X-rays. Because the intensity of the BSE signal is strongly related to the atomic

number (Z) of the specimen, BSE images can provide information about the

distribution of different elements in the sample. For the same reason, BSE imaging

can image colloidal gold immuno-labels of 5 or 10 nm diameter which would

otherwise be difficult or impossible to detect in secondary electron images in

biological specimens. Characteristic X-rays are emitted when the electron beam

removes an inner shell electron from the sample, causing a higher energy electron to

fill the shell and release energy. These characteristic X-rays are used to identify the

composition and measure the abundance of elements in the sample.
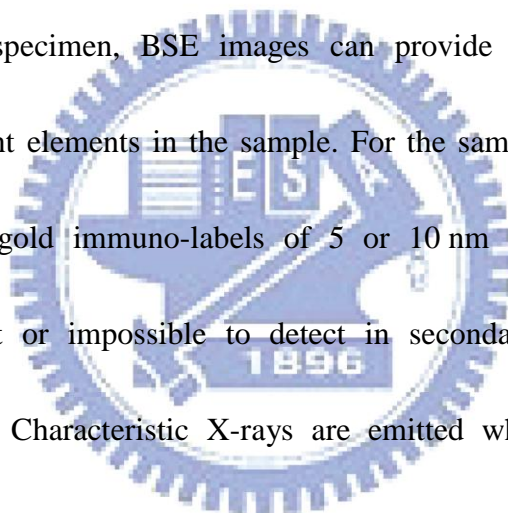
3.3 Photoluminescence

Photoluminescence, a powerful and breakless analysis technology, can reveal the

band structure and the carrier transportation behaviors in a material. Moreover, the

doping type, band gap, composition, etc. of the bulk material or the size, path of

carrier transportation, lifetime, etc. of the nano-material will be shown in the photoluminescence spectrum.

Photoluminescence is a process in which a chemical compound absorbs photons (electromagnetic radiation), transitioning to a higher electronic energy state, and then radiatives photons back out, returning to a lower energy state. The period between absorption and emission is extremely short, on the order of 10 nanoseconds. Light is directed on a sample, where it is absorbed and imparts excess energy into the material in a process called photo-excitation. The luminescence arising from photo-excitation is called photoluminescence (PL). The intensity and spectral content of the photoluminescence is a direct measurement of various important material properties. Fig 3.3.1 shows the schematic setup of PL system with He-Cd laser operating at 30mW at the wavelength of 325nm.
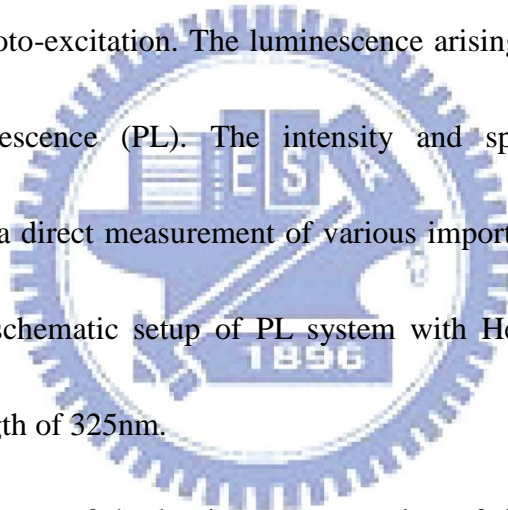
Typically, the process of the luminescence consists of three steps, which is (1) excitation, (2) thermal equilibrium and (3) recombination. Through thermal equilibrium, electron-hole pairs (e-h pairs) generated by incident light recombine and create photon. In the energy band gap, impurities and defects form a variety of energy levels, whose corresponding energy produces radiation through radiative recombination and absorption through non-radiative recombination.
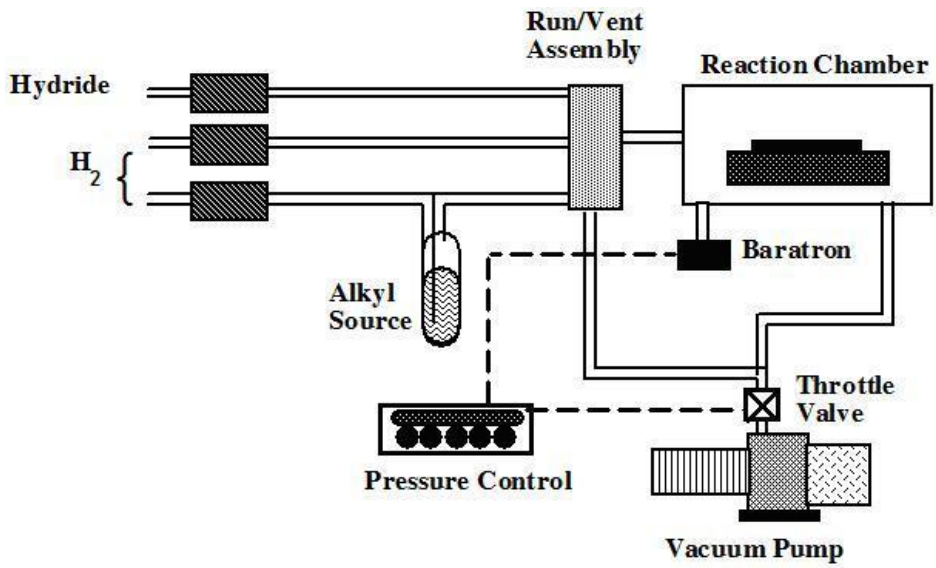
Fig 3.1.1 MOCVD system
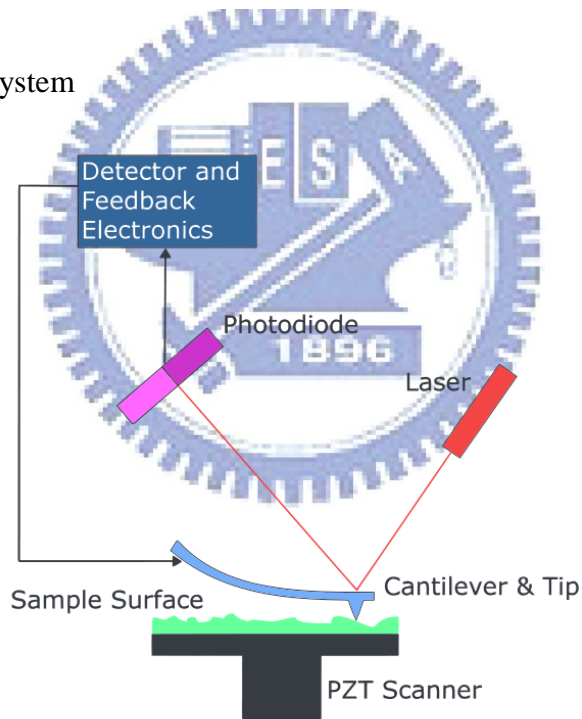
Fig. 3.2.2 Block diagram of atomic force microscope
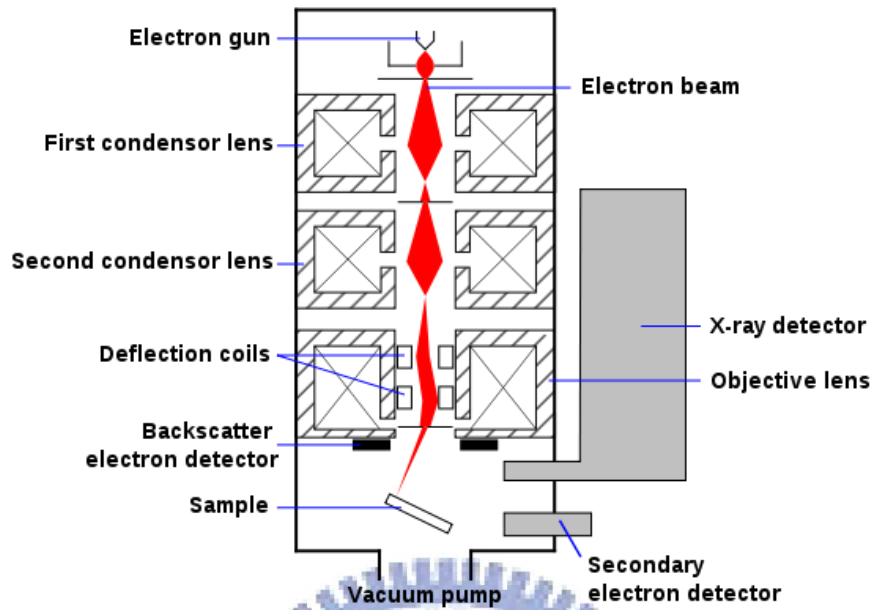
Fig. 3.2.3 Schematic diagram of an SEM
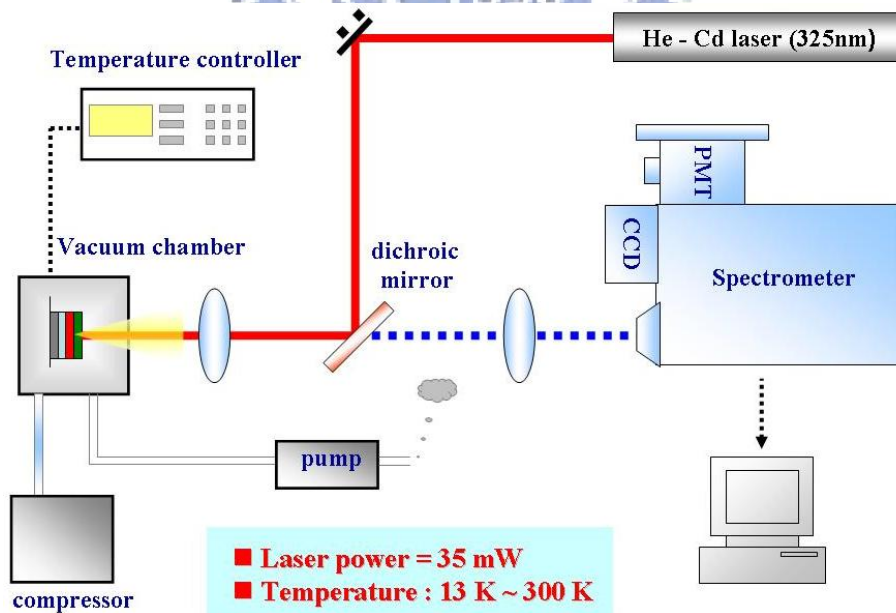
Fig 3.3.1 The schematic diagram of photoluminescence setup

Chapter 4 Optical properties of a-plane $In_{0.2}Ga_{0.8}N$/GaN multiple quantum wells grown on nanorod GaN templates

4.1 Introduction

InGaN-based semiconductors have been used intensively as light emitting diodes (LEDs) and laser diodes (LDs) for their wide band gap through visible to near ultraviolet light spectra [28]. However, the quantum efficiency is reduced in conventional c-plane polar structure, which is due to the existent of the built-in electric field. This built-in electric field would result in decreasing the oscillation strength of the electron-hole pairs and reducing the carrier recombination rate. Recent studies of InGaN/GaN multiple quantum wells (MQWs) demonstrate that it is possible to eliminate such polarization fields along the nonpolar orientation. However, the difficulty to utilize nonpolar GaN is not a suitable substrate for heteroepitaxial a-plane GaN growth. In general, the threading dislocation (TD) density of $\sim 3 \times 10^{10} cm^{-2}$ and a basal stacking fault density of $\sim 3.5 \times 10^5 cm^{-1}$ were commonly observed in a-plane GaN grown on r-plane sapphire. [29] The TDs in GaN act as nonradiative recombination centers which are responsible for poor internal quantum efficiency (IQE). In this thesis, we investigated optical properties of a-plane InGaN/GaN multiple quantum wells with improved GaN template.

In this chapter, we discuss the basic optical characteristics of a-plane

InGaN/GaN MQWs. In section 2, we describe the method how we prepared the samples and had successfully grown five samples with different crystal quality of GaN template. In section 3, we knew the IQE_{PL} (room temperature intensity/ low temperature intensity) and the activation energy fitting result from temperature dependent PL measurement. In section 4, the polarization-dependent PL revealed that the degree of polarization and we simulated strain effect with polarization. In section 5, power dependent PL revealed nonpolar InGaN/GaN MQWs is free from QCSE. In section 6, we present a comparative study of the internal quantum efficiency (IQE) and fit nonradiative coefficient from results.

4.2 Samples preparation and growth

The process of nanorod epitaxial lateral overgrowth (NRELOG) is schematically shown in Fig. 4.2.1. First, a 1.7-um-thick *a*-plane GaN layer was grown on *r*-plane sapphire by metal-organic chemical vapor deposition (MOCVD). Then, a SiO_2 film with a 200 nm thickness and a Ni film with a 10 nm thickness were deposited in sequence to act as the etching mask. Subsequently, the thermal annealing treatment was utilized to obtain nanoscale Ni masks. The diameter of the Ni mask is 300–500 nm and the mask density is estimated to be around 6×10^8 /cm^2 as shown in Fig. 4.2.2. The Ni masks exhibit a random distribution with arbitrary geometries. After that, the GaN nanorods were etched through the nanomask openings by reactive ion etching

(RIE) /inductively coupled plasma etching (ICP) until the height of these nanorods is

0.2, 0.7, 1.2, 1.7 um and 0 um (without nanorod). The etchants for RIE were SF_6 and

Ar, and the etchants for ICP etching were Ar, BCl_3, and Cl_2. Then, the SiO_2 films

were deposited on the nanorods. Since the etching rate of RIE is anisotropic (the

vertical etching rate is faster than horizontal etching rate), we can control the RIE

parameters to remove the SiO_2 on top of a-plane nanorods and the top of nanorods

exhibit the flat a-plane surface. Because the nanorods were fabricated via Ni masks,

the shape and homogeneities of nanorods was similar to that of Ni masks. Finally, the

GaN regrowth was performed on the nanorod template by MOCVD.

Figures 4.2.3 show the 9 um^2 atomic force microscopy (AFM) images of the

as-grown sample and the NRELOG samples, respectively. These samples were grown

under the same growth conditions (the growth temperature, pressure, and V/III ratio

were 1180 ℃, 200 mbar, and 800–900, respectively). Compared with the as-grown

sample, the NRELOG samples apparently had the superior surface quality and less

surface pits when the depth of nanorod is deeper. It is believed to be originated from

the TD terminations with the surface. [29] Therefore, the less surface pits show the

possibility of dislocation reduction. The rms roughness of the NRELOG sample was

approximately 1.39 nm in 1.7um sample, which was smaller than that of the as-grown

sample (nearly 4.04 nm).

Then, as shown in Fig. 4.2.4, 6 pairs of 60 Å -thick InGaN well / 180 Å -thick GaN

barrier MQW were grown on all templates. We prepared five groups of MQW with

the same condition. The anisotropic strain within nonpolar structures results in more

complex Poisson ratio. Although there are many researches about a-plane structures,

the Indium composition of the a-plane InGaN/GaN MQWs still could not be

calculated precisely. The X-Ray th / 2th scan of a-plane InGaN / GaN MQWs

analysis confirmed that the Indium compositions are about 20%. Micro-structural

characterization was carried out using the plan-view TEM images of the a-plane GaN

film regrown on 1.7-µm-height nanorods in Fig.4.2.5 and the average TDD was

estimated to be 1×10^9 cm^{-2}, which was about 1~2 orders magnitude lower than that

in as-grown GaN (3×10^{10} cm^{-2}). Typical bright-field cross-sectional TEM image of

the a-plane In$_{0.2}$Ga$_{0.8}$N/GaN MQWs on 1.7-µm-height nanorods was shown in Fig.

4.2.6.

4.3 Temperature dependent photoluminescence a-plane InGaN/GaN MQWs

We want to know the optical properties of a-plane InGaN/GaN MQWs grown on

nanorod GaN templates including the carrier confinement and the activation energy, we

performed the temperature-dependent photoluminescence from 40 to 300K.

Fig. 4.3.1 shows the evolution of PL spectra as a function of temperature for the

a-plane InGaN/GaN MQWs. We can clearly observe two peaks existing at 40 K. The

partial phase segregation and composition inhomogeneity would result in exciton localization within some indium-rich regions. [30] The low-energy peak existed from 40 to 300 K referred to the signal come from MQWs, and the high-energy peak merged at high temperature referred to the signal from shallow localized states.

The decrease of PL intensity with increasing temperature is observed. Thermal quenching PL intensity with increasing temperature is a general phenomenon in semiconductor nanostructure which is caused by carriers thermalization from the radiative recombination centers or/and localized states to the nonradiative recombination centers or/and delocalized states. Temperature-dependent PL was utilized to investigate the quantum efficiency of the grown samples. In general, the temperature-induced quenching of luminescence involves the thermal activation of excitons to nonradiative defect states. [31] In other words, a slower intensity decline with the temperature increasing means a lower defect density in the grown sample. The normalized integrated PL intensity ratio obtained at 40 and 300 K $I_{PL}(300k)/I_{PL}(40k)$ in Table 4.3.1 could represent the IQE of the InGaN/GaN MQWs samples. The IQE obtained from $I_{PL}(300k)/I_{PL}(40k)$ value are sequent 0.1 (0um), 0.15 (0.2um), 0.27 (0.7um), 0.28 (1.2um) and 0.35 (1.7um). As we can see, the internal quantum efficiency increased with the depth of nanorod template and had an optimized value with 1.7um. The IQE for the 1.7um NRELOG GaN template has 3.5

times increase compared to that of the as-grown GaN. The reduction in the TD

density in case of NRELOG samples as compared to as-grown samples can contribute

to the enhancement in the quantum efficiency. [32]

Fig. 4.3.2 shows the normalized integrated PL intensity of InGaN/GaN MQWs

emission as a function of 1000/T for the as-grown sample and the NRELOG samples.

It has been studied that the carrier could receive activation energy to thermalize from

the potential minima, the radiative or localized centers, to nonradiative or delocalized

centers as the temperature is increased. [33] Therefore, it is expected that the deeper

localization with better confinement should have larger activation energy. In order to

further verify that, the experimental temperature-dependent PL data were fitted by

Arrhenius equation to investigate the carrier behavior during the thermal processes,

[34]
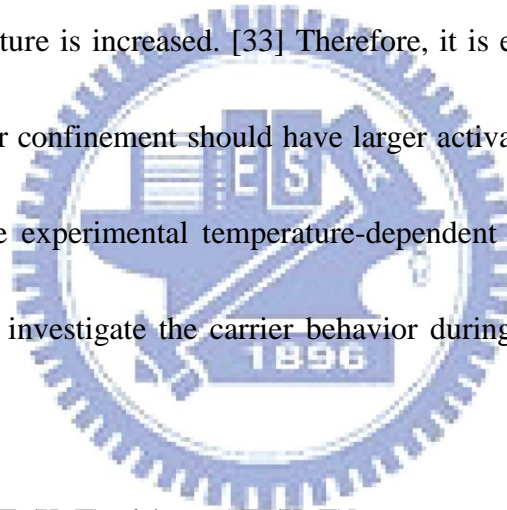
$$I\ (T) = I_0/\ [1+a*exp\ (-E_a/K_BT) +b*exp\ (-E_b/K_BT)] \qquad\qquad Eq.\ (4.3.1)$$

where $I(T)$ is the temperature-dependent PL intensity, I_0 is the PL intensity at 40 K, K_b

is Boltzmann's constant, A and B are the rate constants, and Ea and Eb are the

activation energies for two different nonradiative channels, which can be

distinguished for the high temperature and low temperature region. [35] The fitted

activation energy of the five samples is listed in Table 4.3.2. As expected, the

activation energy gradually increases and reaches the maximum value of 135 meV

when nanorod depth is 1.7um. The trend of the activation energy is consistency with the internal quantum efficiency. It is believed that the carrier confinement would improve when the nanorod depth is deeper. Because the quality of a-plane GaN films was improved by using nanorod GaN template and it was better when nanorod depth was deeper.

In addition, the evolution with temperature of the peak shift of MQWS peak energy for the five samples investigated here is given in Fig. 4.3.3, where the peak positions at 40 K are the reference. The peak shift of PL varies as a function of temperature from 40 to 300 K and exhibits a continuous redshift.

4.4 In-plane polarization effect of a-plane InGaN/GaN MQWs emission

In nonpolar InGaN/GaN MQWs, the anisotropic biaxial strain attributed to the low symmetry of its structures. In this section, we performed a polarization-dependent PL measurement at 300 K to investigate the effects of GaN templates on the polarization characteristics. The PL measurement was excited using the 325 nm He-Cd laser and a rotational polarizer was placed in front of the entrance slit of the spectrometer. The schematic of our experimental setup for the PL measurement is shown in Fig. 4.4.1. We varied the polarization in [11-20] a-plane from 0$^\text{o}$, parallel to the m-axis (E$\perp$C), 0° to 90°, parallel to the c-axis (E//C). The coordinate system used here is shown in Fig. 2.4.1.

Fig. 4.4.2(a) shows the room temperature polarization-dependent PL spectra with

nanorod GaN templates varied from 0um to 1.7um and the polarization angles from 0°

to 90° divided by 15°. In order to understand the emission intensity on polarization

angels, the symmetric of normalized PL intensity versus the polarization degree from

0° to 360° was also illustrated in Fig. 4.4.2(b).

The polarization degree ρ is defined as

$$\rho = (I_{\perp} - I_{\parallel}) / (I_{\perp} + I_{\parallel}) \hspace{3cm} \text{Eq. (4.4.1)}$$

, where I$\perp$ and I// are PL intensities represented for E$\perp$C and E//C. The polarization

degree ρ of our samples are sequent 85, 81, 65, 60 and 53 % for 0, 0.2, 0.7, 1.2 and

1.7um nanorod depth at 300 K. Here, only the low energy peak of InGaN/GaN

MQWs, which was dominant in the luminescence mechanism from 300 K, was

discussed and the results were listed in Table 4.4.1. The experiment results show that

the polarization degree and peak energy shift (ΔE) was decreasing when the etching

depth of nanorod was increasing. In addition, we also investigated the effect of

different nanorod depth on the polarization degree.

In Fig. 4.4.3, the polarization ratio was plotted as the function of etching depth of

nanorod. From data of the polarization ratio and peak energy shift, we could infer that

the strain, carrier density and scattering are reasons. And strain might be the main

reason. Using process of lateral overgrowth on nanorod templates could decrease

contact area with sapphire as regrowth. In addition, the strain would be relaxed [12]

with increasing nanorod depth. We have known that the crystal quality of *a*-plane

GaN films was improved by using epitaxial lateral overgrowth on a nanorod GaN

template by AFM and TEM. We think the compressive strain of *a*-plane InGan/GaN

MQWs would be alleviated with nanrod depth. And we prove our thoughts through

simulation; the voids in GaN template were more when the nanorod depth is deeper,

so the effect of scattering was more obvious.

According to simulation, the injection carrier density and the strain would affect

polarization degree. From Eq. (4.4.2),

$$G = P_{laser}(1-R)\alpha l /(A_{spot}lh\nu) = P_{laser}(1-R)\alpha /(A_{spot}h\nu) \qquad \text{Eq. (4.4.2)}$$

$$G = R_{total} = An + Bn^2 \qquad \text{Eq. (4.4.3)}$$

the generation rate was identical at the same power in our experiments. The fitting

results in Chapter 4.6, we knew that the value of $A_{1.7um}$ was the smallest than other

samples when B was the same. So the injection carrier density was the biggest in 1.7um

and was the smallest in 0 um. Fig 4.4.4 Simulated polarization degree with different

injection carrier density of $In_{0.25}Ga_{0.75}N/GaN$ MQWs at 300K. PL spectrum simulated

as a function of x'-polarized and y'-polarized of $In_{0.25}Ga_{0.75}N/GaN$ MQWs at 300K

varied strain from 1 time to 2 times in Fig. 4.4.5 and we supposed the injection current

density was 5×10^{18} cm^{-3}. The polarization degree and peak energy shift (ΔE) was

increasing when the strain was increasing. The trend of simulation in Fig. 4.4.6 is

consistency with the experiment.

4.5 Nonpolar characteristics of a-plane InGaN/GaN MQWs

In conventional *c*-plane polar structure, the built-in field with the MQWs would

lead to band tilting. If the photo-genarated carriers were injected into the MQWs, the

built-in electric field could be screened and result in a blue-shift of PL energy peak

[36]. As we mentioned above, the useful approach for reducing the built-in electric

field is to grown MQWs along the nonpolar direction. In this section, we performed

the power dependent photoluminescence to realize the built-in field influence on our

samples.

The power dependent photoluminescence was demonstrated by using He-Cd

laser operated at 325 nm. The excitation power increased from 5uW to 35 mW. Fig.

4.5.1 shows the PL spectra as a function of excitation power for our five samples with

different nanorod depth at room temperature. As our previous work on *c*-plane

MQWs, increasing the Indium composition would result in larger PL peak blue-shift

as the In composition was increased, which is known to due to larger built-in electric

field [37]. On the contrary, the wavelength un-shift was observed of our five samples

during the power-dependent PL measurement as shown in Fig. 4.5.2. The unchanged

PL peak energy revealed that the structure was free from QCSE when we grown our
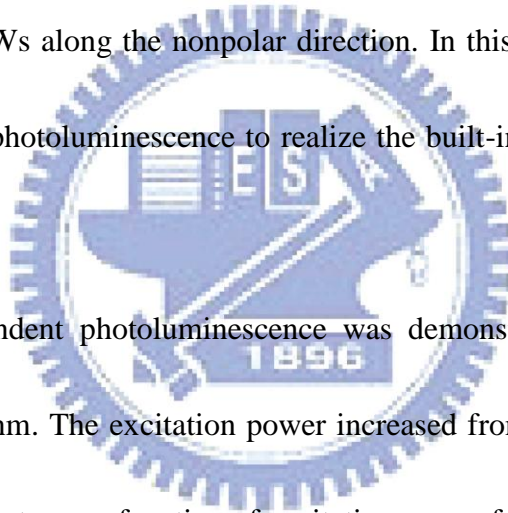
samples along nonpolar *a*–plane directions.

In addition, we also investigated the excitation power dependence on luminescence intensity. Fig. 4.5.2 shows the relation between excitation power density and the integrated PL intensity. The results were fitting based on the relation I~P^{α} where I is the integrated PL intensity, P is the excitation power density and α is the power index. In the case of *c*-plane MQWs, the superlinear relation (α>1) due to decreasing nonradiative recombination with photo-injected carriers has been observed [36]. The α factors of our samples were approximate 1. The linear relation of these four samples (α~1) indicated the nonradiative channels saturate and radiative recombination predominates. Therefore, it can be concluded that the QCSE was absent in our samples.
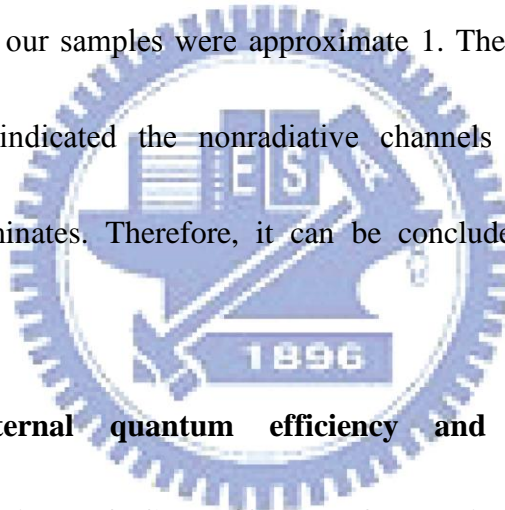
4.6 Measuring internal quantum efficiency and fitting nonradiative recombination coefficient of GaInN/GaN MQWs with different dislocation densities

PL was measured with changing excitation power density at 300 and 20 K on the same point. [38] A 325 nm He-Cd laser was used to excite all samples consistently, which have nominally the same structure, except for the nanorod depth of GaN template. The excitation power density at the sample surface was changed from 0.05 W/cm^2 to 300 W/cm^2. Figure 4.6.1 shows relative PL quantum efficiency for both

samples at 20 and 300 K. Curves are normalized by the peak value at 20 K for both

samples. We assume peak PL efficiency at 20K is 100% and correspond to IQE curve

for both samples at 20 and 300 K plots in Fig. 4.6.1. At 300 K, the 1.7um sample

shows a higher efficiency than the as-grown sample and the IQE of a-plane

InGaN/GaN MQWs are approximately 39% (1.7um), 30% (1.2um), 26% (0.7um),

16% (0.2um), and 13%(0um), respectively. In the present experiment, a 325 nm

He-Cd laser was used and this excites above the GaN bandgap energy. Therefore,

there is a possibility that the carrier excited at the GaN barrier layer contributed to PL,

especially at LT. [39] This makes measured IQE at RT somewhat higher than the

actual case. Fortunately, this condition was not obvious in our data at 20k (Fig 4.6.2)

and 300k (Fig 4.5.1).
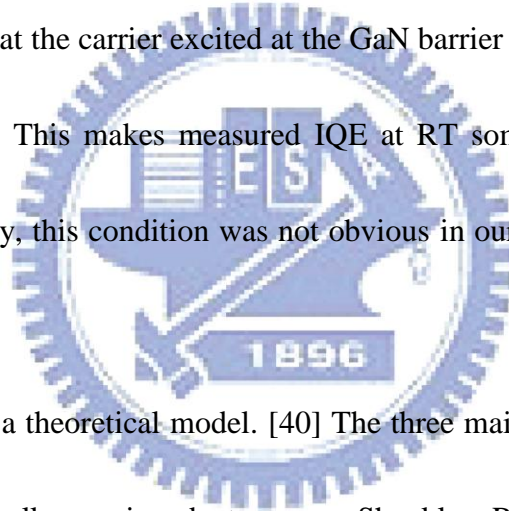
Next, we present a theoretical model. [40] The three main carrier-recombination

mechanisms in a bulk semiconductor are Shockley–Read–Hall nonradiative

recombination, expressed as An, bimolecular radiative recombination Bn^2, and Auger

nonradiative recombination Cn^3, where A, B, and C are the respective recombination

coefficients and n is the carrier concentration. Auger recombination affects LED

efficiency only at very high excitation; In our experiments, the generation rate and the

IQE at steady state can be expressed as

$$G = R_{total} = An + Bn^2 + Cn^3$$

$$IQE = \frac{Bn^2}{An + Bn^2 + Cn^3} = \frac{Bn^2}{G}$$

Eq. (4.6.2)

and the integrated PL intensity can be expressed as

$$I_{PL} = \eta B n^2 \hspace{4cm} \text{Eq. (4.6.3)}$$

where η is a constant determined by the volume of the excited active region and the

total collection efficiency of luminescence. By eliminating n in Eqs. (4.6.1) and

(4.6.3), we can express the generation rate in terms of integrated PL intensity

$$G = \frac{A}{\sqrt{B\eta}}\sqrt{I_{PL}} + \frac{1}{\eta}I_{PL} + \frac{C}{(\eta B)^{1.5}}I_{PL}^{1.5} \hspace{2cm} \text{Eq. (4.6.4)}$$

The connection between theory and experiment is completed by noting that the

generation rate can be separately calculated from experimental parameters using

$$G = P_{laser}(1-R)\alpha l /(A_{spot}lh\nu) = P_{laser}(1-R)\alpha /(A_{spot}h\nu) \hspace{1cm} \text{Eq. (4.6.5)}$$

where P_{laser} is the peak optical power incident on the sample, R (18%) is the Fresnel

reflection at the sample surface, l (36nm) is the total thickness of the GaInN QWs,

A_{spot} (1.2×10^4 um^2) is the area of the laser spot on the sample surface, $h\nu$ (2.75 eV) is

the energy of a 451 nm photon, and (5.7 um^{-1}) is the absorption coefficient of the

Ga$_{0.8}$In$_{0.2}$N well at 451 nm. Fig 4.6.3 shows the experimental results for G as a

function of I_{PL} obtained using Eq. (4.6.5) and our previous fits of the spectral data.

Using Eq. (4.6.4) to fit the experimental data in Fig. 4.6.3, we then obtain the

coefficients $P_1 = A(B\eta)^{-1/2}$,$P_2 = 1/\eta$ and $P_3 = C(B\eta)^{-3/2}$. Because the samples have the

same layer structure and are measured under the same conditions, the values of P_2 (or

η) for the three samples should be the same or similar. Therefore we keep the values

of P_2 fixed for the three samples while fitting the data. The fitted results, also shown

in Fig. 4.6.3, are excellent; thus Eq. (4.6.4) appears to accurately model our

experiments.

If one assumes a value of B at room temperature of $1 \times 10^{-11} \text{cm}^{-3} \text{s}^{-1}$ for nonpolar

[41] , the value of carrier concentration n can also be obtained. By eliminating η from

the two coefficients P_1, P_2 and P_3, one can obtain the value of $A(B)^{-1/2}$ and finally, the

coefficient A. Considering the fact that B is known to only one significant figure, the

accuracy of A and n are similarly limited.

Figure 4.6.4 shows the measured nonradiative coefficient A as a function of

nanorod etching depth, and the measured nonradiative recombination coefficient A

varied from 1.9×10^7 to $4.1 \times 10^6 \text{ s}^{-1}$ in Table 4.6.1 as the etching depth increases from

0 to 1.7 um. From the TEM images in Fig. 4.2.5, the average threading dislocation

density was estimated to be $1 \times 10^9 \text{ cm}^{-2}$, which was about 1~2 orders magnitude lower

than that in as-grown GaN ($3 \times 10^{10} \text{ cm}^{-2}$). The data in Fig. 4.6.4 indicate that the

threading-dislocation density significantly affects the GaInN MQW efficiency, which

supports the argument that threading dislocations behave as nonradiative

recombination centers. [42] An upper limit for the Auger coefficient C is estimated to

be about $1 \times 10^{-30} \text{ cm}^6 \text{ s}^{-1}$ for GaInN material and the actual value may be smaller. [43]
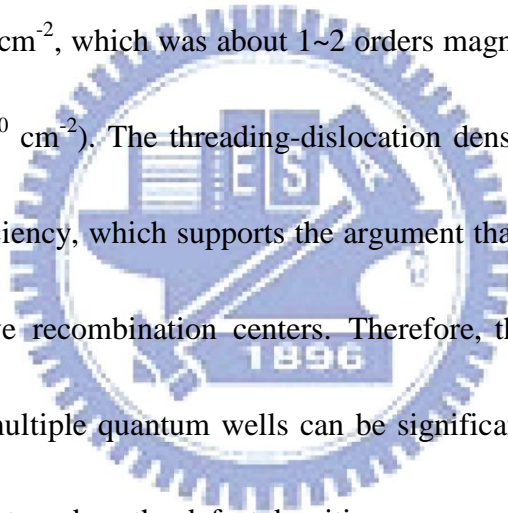
Therefore in our experiments, the Cn^3 term is much less than the Bn^2 term considering that the carrier concentration in our experiments is less than 5×10^{18} cm^{-3}. So we didn't take into consideration with Auger coefficient C.

At the highest excitation, which has a generation rate of 5×10^{25} cm^{-3} s^{-1}, the IQEs are 43%, 36%, 29%, 19% and 15% for samples 1.7um, 1.2um, 0.7um 0.2um and 0um, respectively. Moreover, we compared the internal quantum efficiency of fitting value with experimental value in Fig. 4.6.5. According to the figure, we know that fitting values were consistent with experimental values.

4.7 Conclusion

In conclusion, we investigated a-plane InGaN/GaN multiple quantum wells were grown on r-plane sapphire by metal organic chemical vapor deposition. The crystal quality of *a*-plane GaN films was improved by using epitaxial lateral overgrowth on a nanorod GaN template by AFM and TEM. Temperature dependent PL clearly showed the internal quantum efficiency increased with the depth of nanorod template and had an optimized value with 1.7um. As expected, the activation energy gradually increases and reaches the maximum value of 135 meV when nanorod depth is 1.7um. The trend of the activation energy is consistency with the internal quantum efficiency. The experiment results show that the polarization degree and peak energy shift (ΔE) was decreasing when the etching depth of nanorod was increasing. We could infer

that strain is an important reason and prove our thoughts through simulation. No built-in electric field was observed in the power dependent PL measurement for all samples. The IQE of a-plane InGaN/GaN MQWs are approximately 39% (1.7um), 30% (1.2um), 26% (0.7um), 16% (0.2um), and 13%(0um) using PL with changing excitation power density at 300 and 20 K. The measured nonradiative recombination coefficient A varied from 1.9×10^7 to 4.1×10^6 s^{-1} as the etching depth increases from 0 to 1.7 um. From the TEM images, the average threading dislocation density was estimated to be 1×10^9 cm^{-2}, which was about 1~2 orders magnitude lower than that in as-grown GaN (3×10^{10} cm^{-2}). The threading-dislocation density significantly affects the GaInN MQW efficiency, which supports the argument that threading dislocations behave as nonradiative recombination centers. Therefore, the optical properties of a-plane InGaN/GaN multiple quantum wells can be significantly improved by using nanorod GaN template to reduce the defect densities.
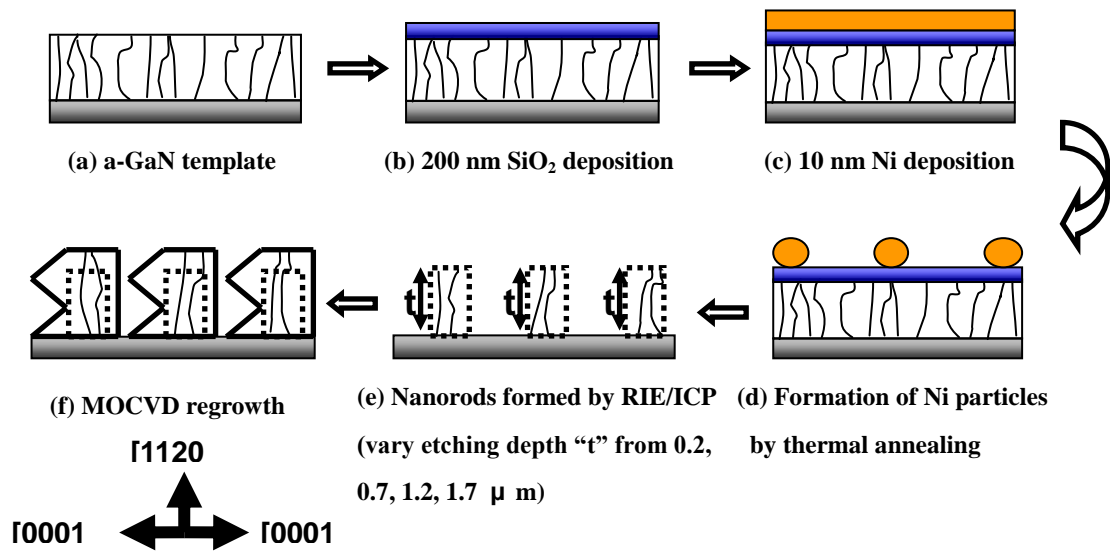
(a) a-GaN template   **(b) 200 nm SiO$_2$ deposition**   **(c) 10 nm Ni deposition**

(f) MOCVD regrowth   **(e) Nanorods formed by RIE/ICP**   **(d) Formation of Ni particles**

Γ1120

Γ0001   Γ0001

(vary etching depth "t" from 0.2,   **by thermal annealing**

0.7, 1.2, 1.7 μm)

Fig. 4.2.1 (Color online) Flow chart of *a*-plane GaN NRELOG process.

(a) nanorods   500 nm

(b) [0001] [0001]   1μ m

(c) Ga-face N-face   [112̲0] [11̲00] [0001]   1μ m
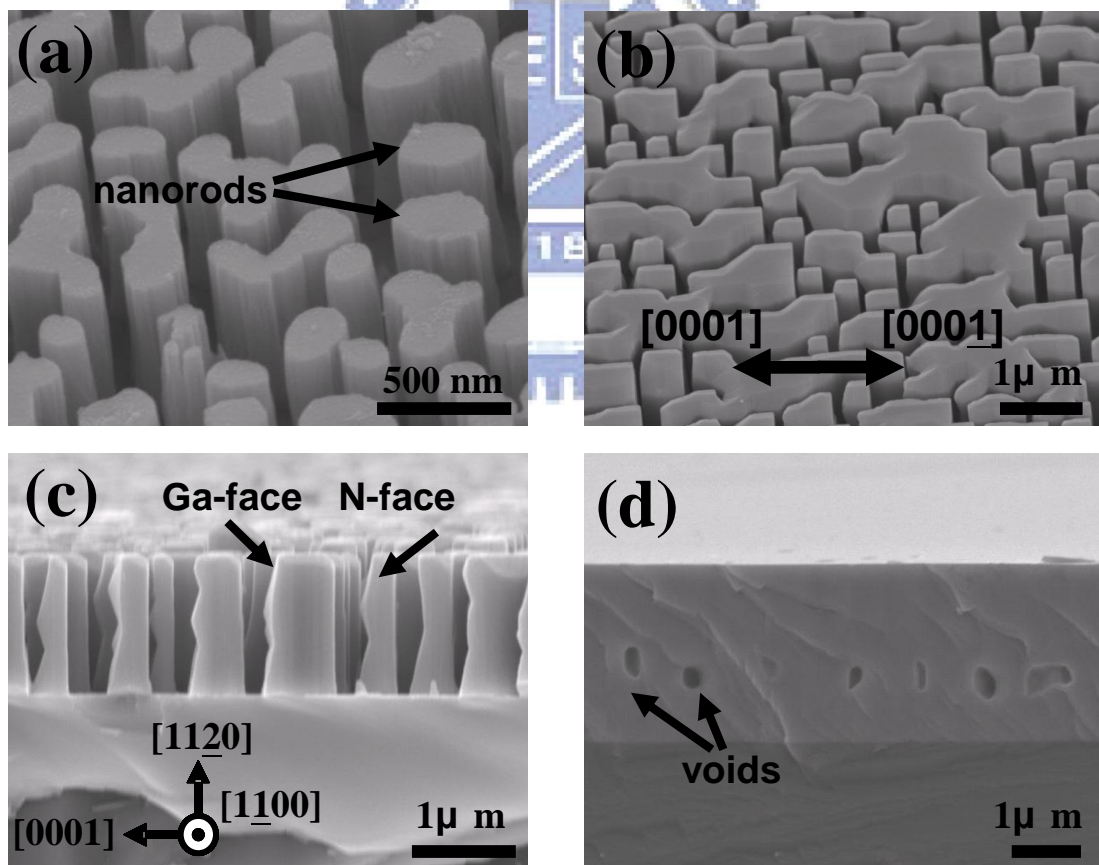
(d) voids   1μ m

Fig. 4.2.2 (Color online) SEM images of (a) Fabricated GaN nanorods. (b) Mask

density of GaN template. (c) Initial MOCVD regrowth on *a*-plane GaN nanorods in

90° angle of view, and (d) fully coalesced *a*-plane GaN films in cross-sectional view.
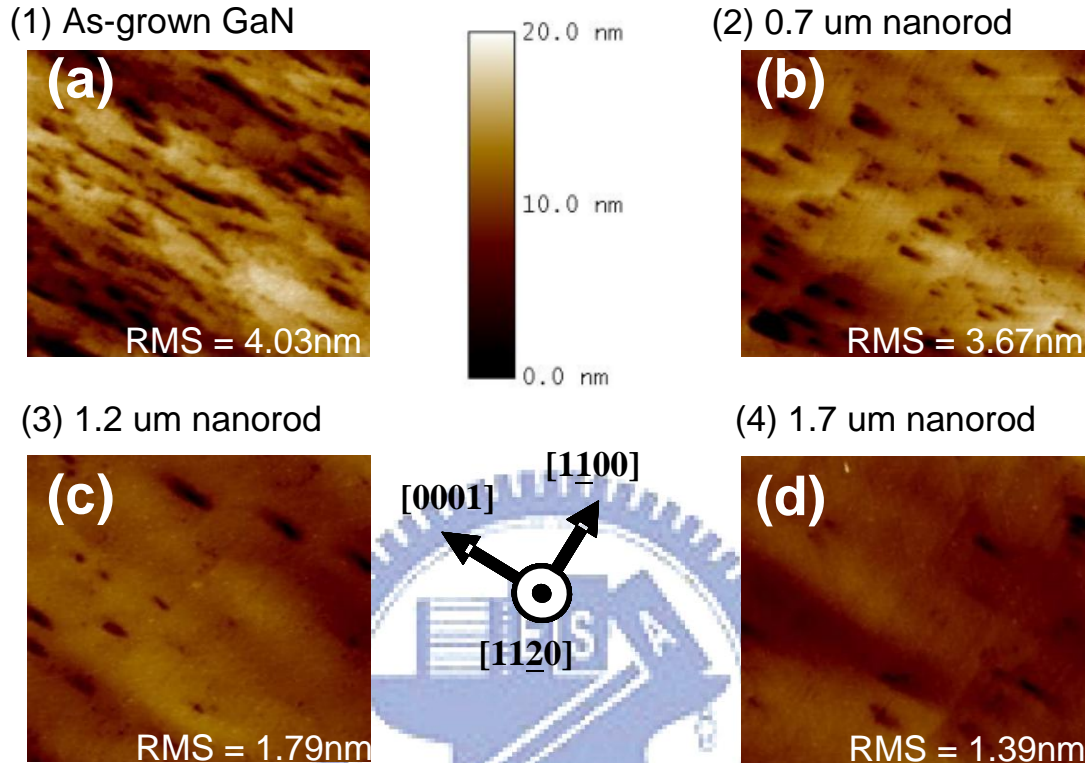
(1) As-grown GaN

(2) 0.7 um nanorod

(3) 1.2 um nanorod

(4) 1.7 um nanorod

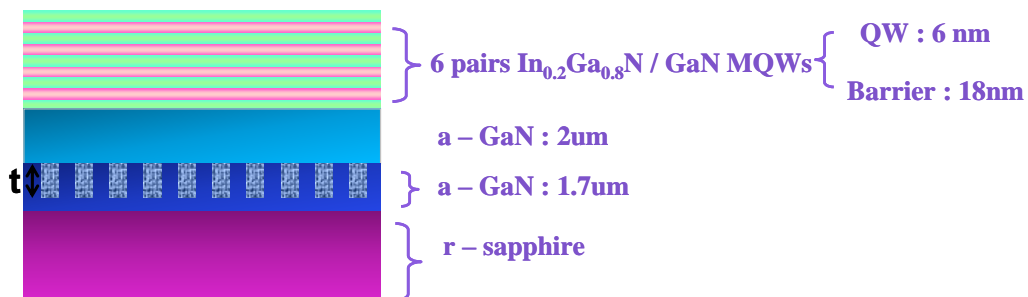Fig. 4.2.3 9 um^2 AFM images of the as-grown sample and the NRELOG sample, respectively.
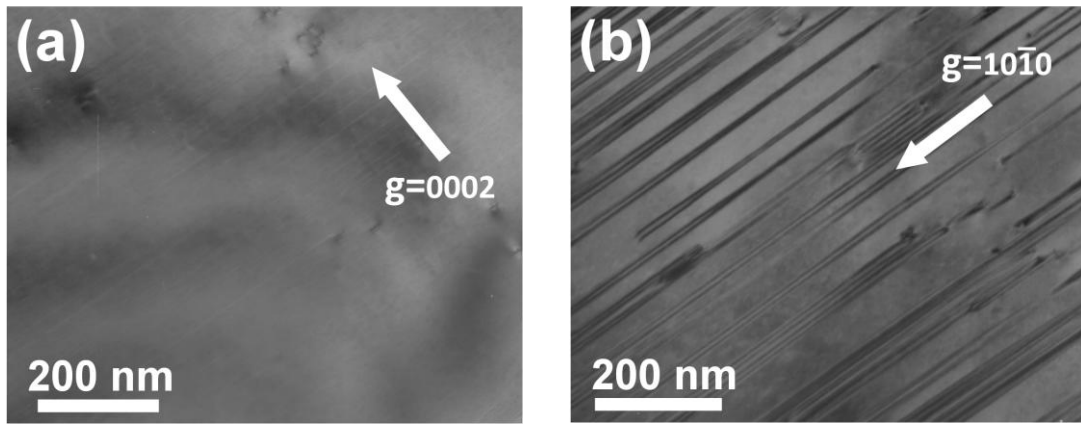

Fig. 4.2.4 The schematic drawing of sample structure.

Fig. 4.2.5 The plan-view TEM images of the a-plane GaN film regrown on 1.7-μm-height nanorods as observed with (a) g=0002 to observe dislocations, and (b) g=10$\bar{1}$0 to observe stacking faults.
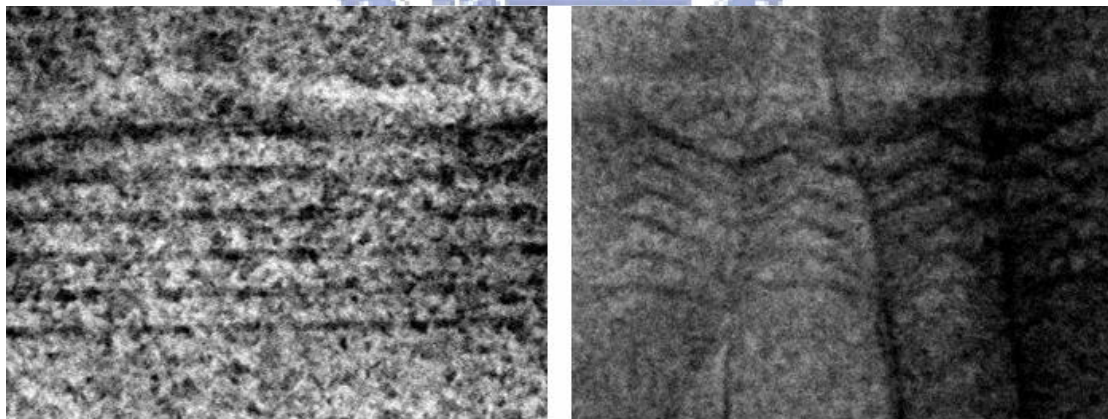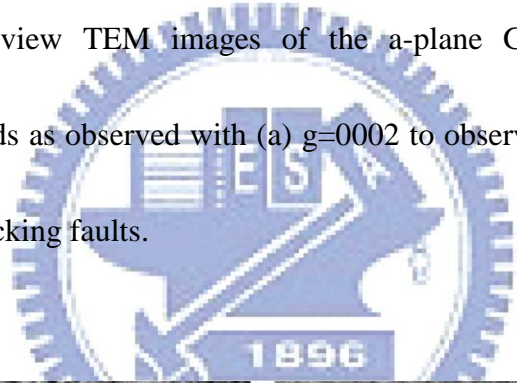

Fig. 4.2.6 Typical bright-field cross-sectional TEM image of the a-plane InGaN/GaN MQWs on 1.7-μm-height nanorods (a) MQWs in better region. (b) the region in higher threading dislocation density.
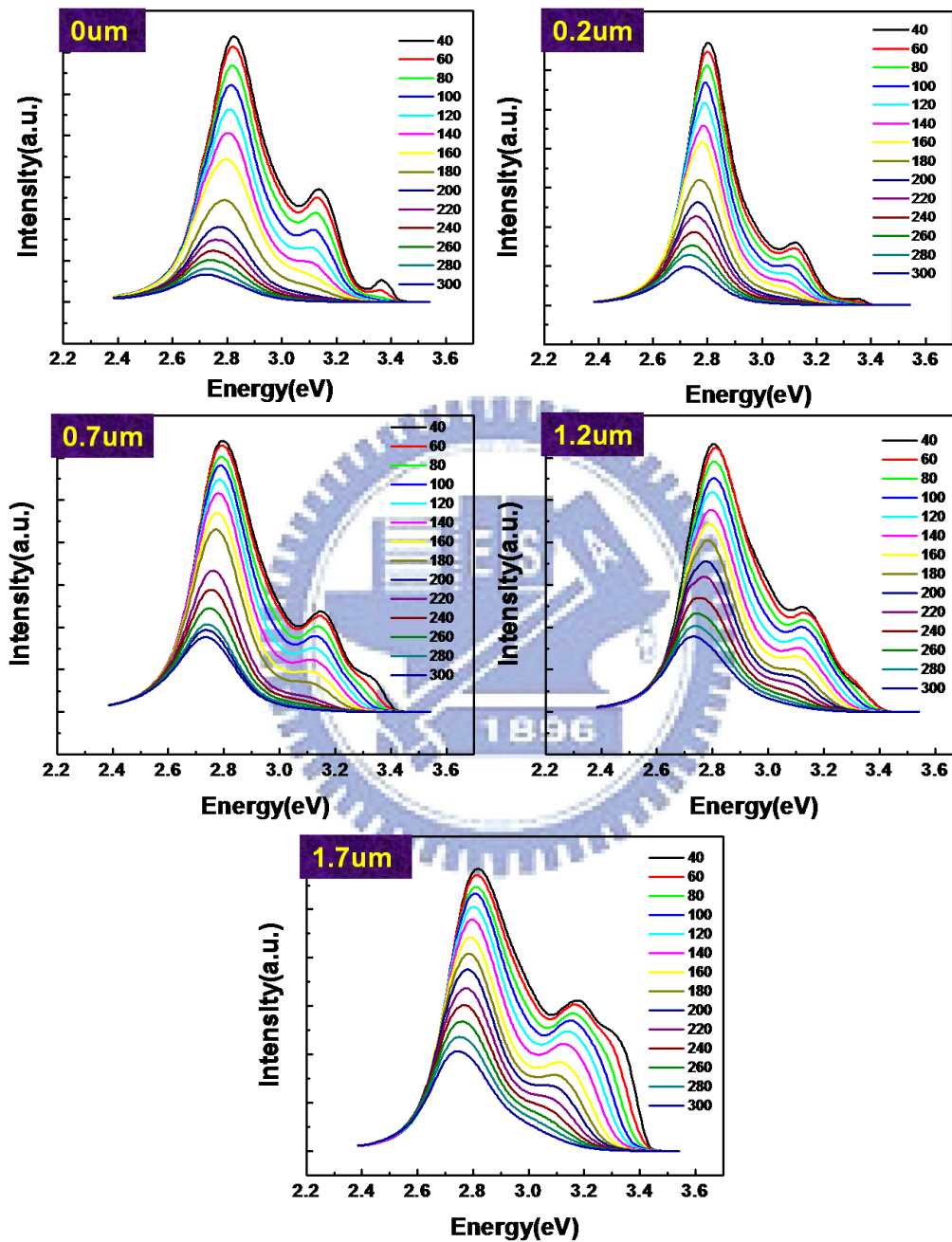
Fig. 4.3.1 (Color online) The PL emission spectra under temperature varied from 40

to 300 K. They imply the samples with nanorod templates varied from 0um to 1.7um.

Nanorod depth	0um	0.2um	0.7um	1.2um	1.7um
$I_{PL}(300k)/$ $I_{PL}(40k)$	0.108	0.147	0.276	0.283	0.35

Table 4.3.1 The experimental results represent the IQE of the InGaN/GaN MQWs samples of *a*-plane InGaN/GaN MQWs.
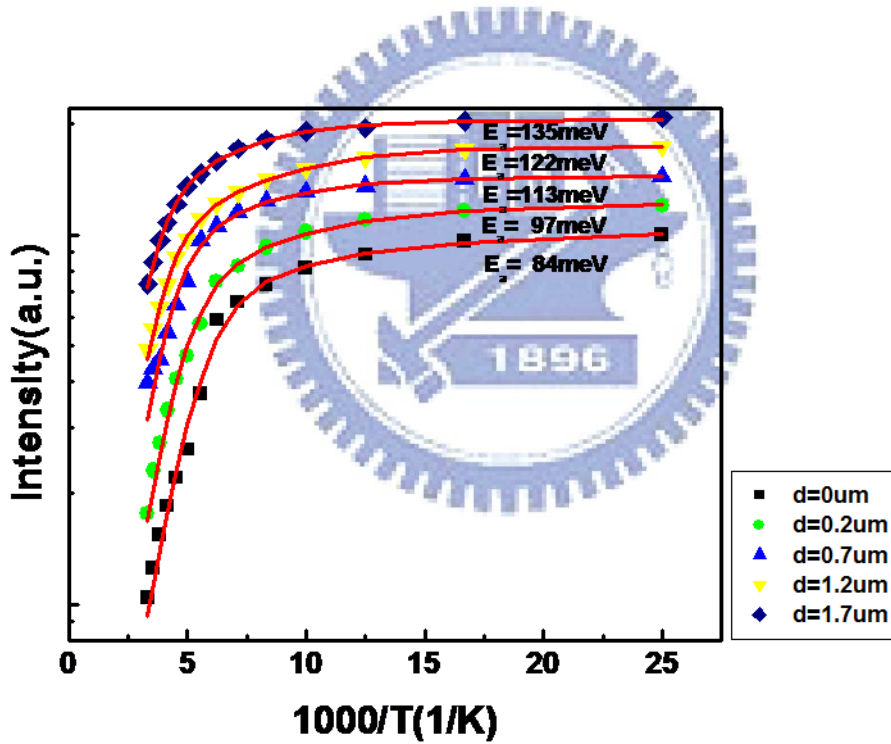

Fig. 4.3.2 (Color online) The normalized PL intensity plotted as a function of $1/T$ for the samples with different nanorod depth. The symbols stand for the measurement results and the solid line means the fitted curve of the five samples. The number labeled near the curves represents the fitted activation energies.

	0um	0.2um	0.7um	1.2um	1.7um
E_a(meV)	84.3	96.9	112.9	122	134.8
E_b(meV)	14.5	18.5	24	23.1	29.2

Table 4.3.2 The fitting results of activation energy of *a*-plane InGaN/GaN MQWs

with different nanorod depth.
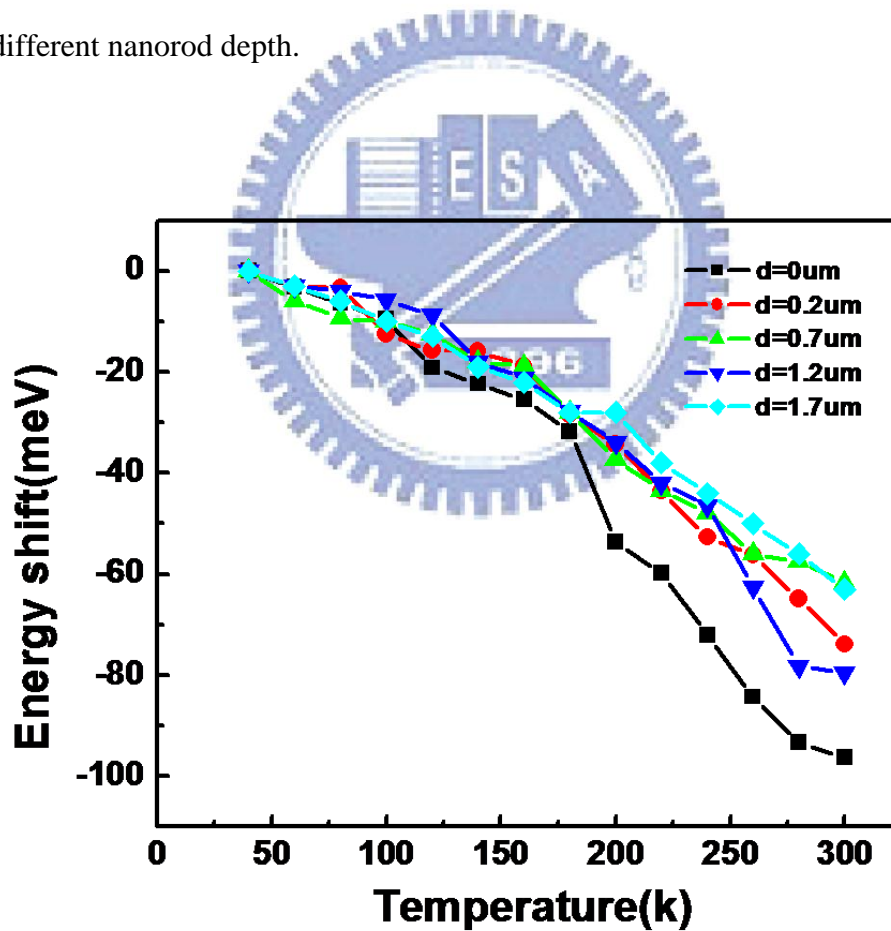
Fig. 4.3.3 The temperature-dependent PL results of the five samples shows the

dominate wavelength shift from 20 to 300 K.
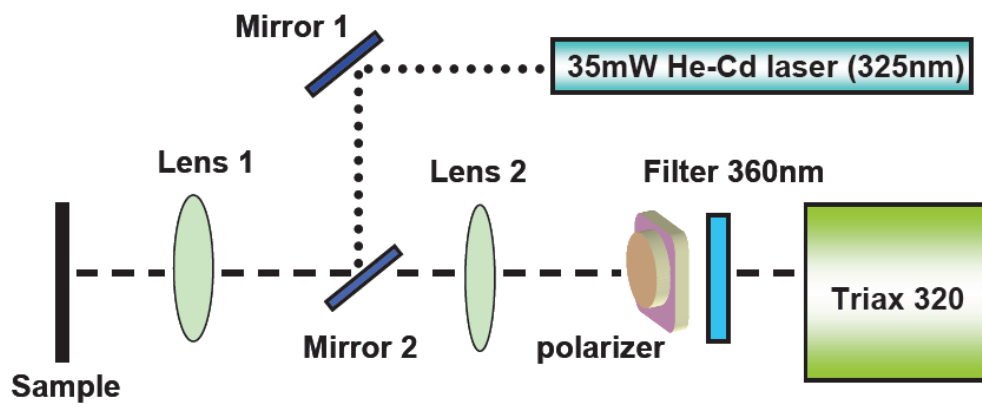
Fig. 4.4.1 The schematic of experimental PL setup for the in-plane polarization
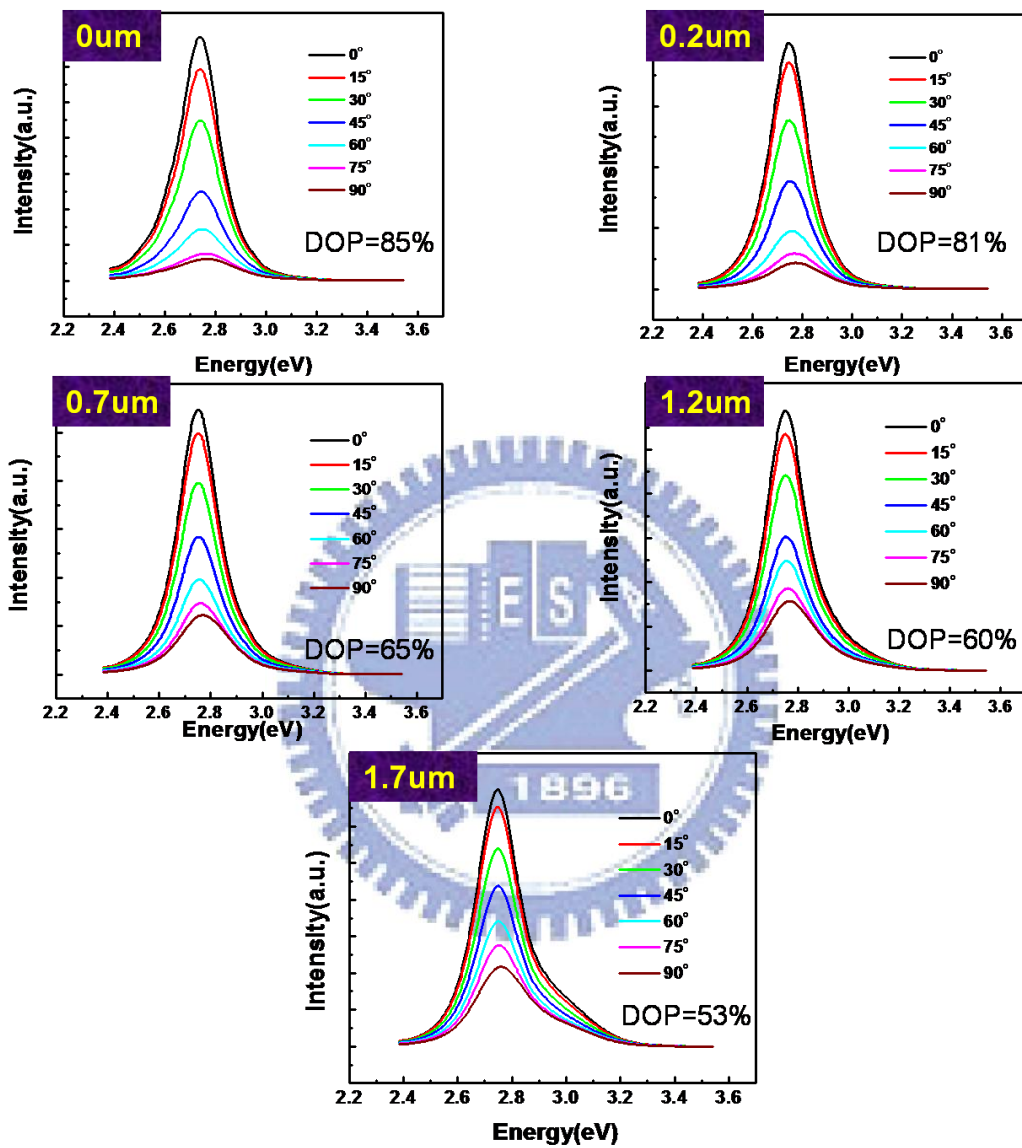
Fig. 4.4.2 (a) Room temperature polarization-dependent PL spectra for polarization

angles from 0° to 90° with nanorod templates varied from 0um to 1.7um.
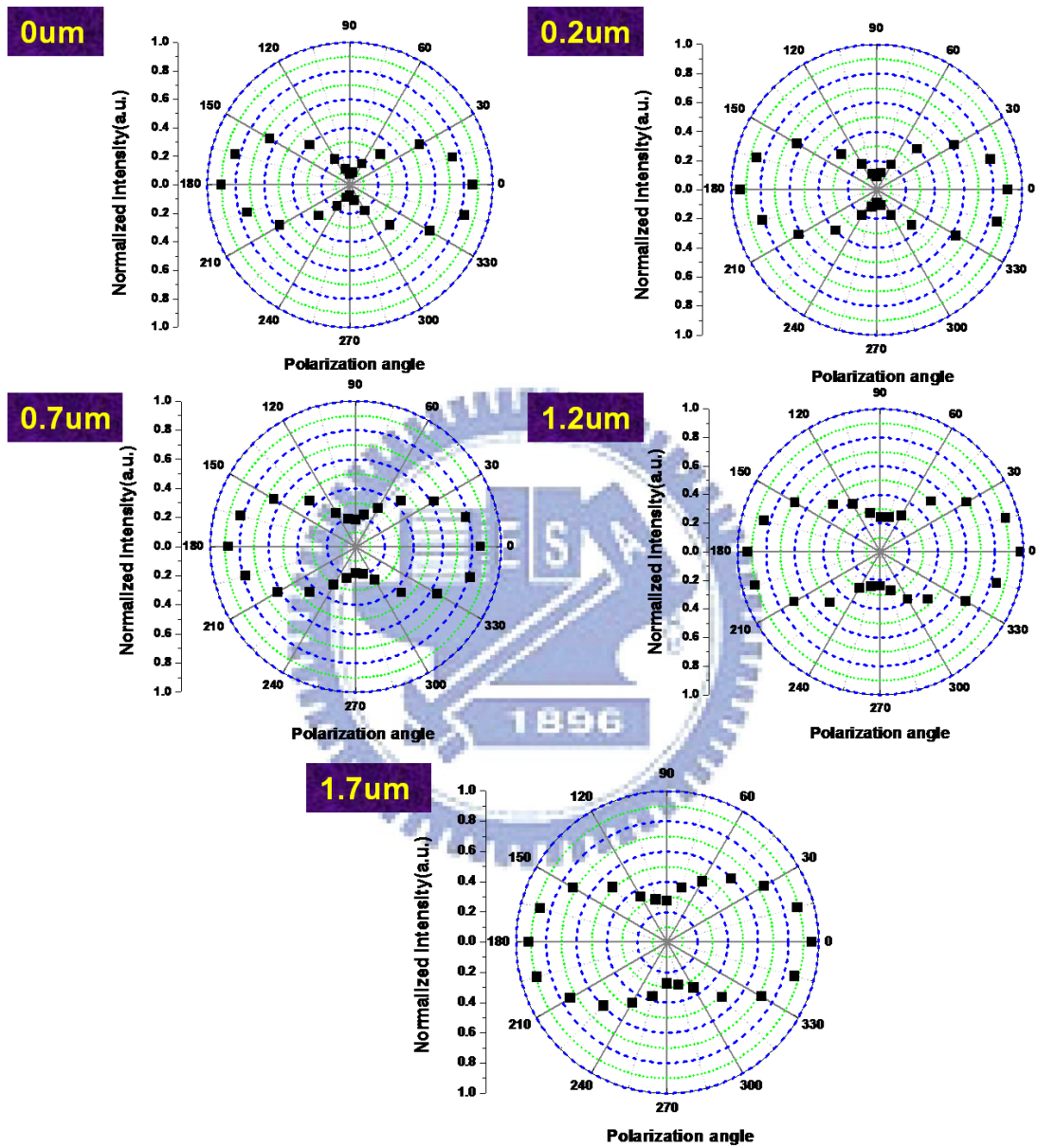
Fig. 4.4.2 (b) The symmetric of normalized PL intensity versusbthe polarization degree from 0° to 360°.
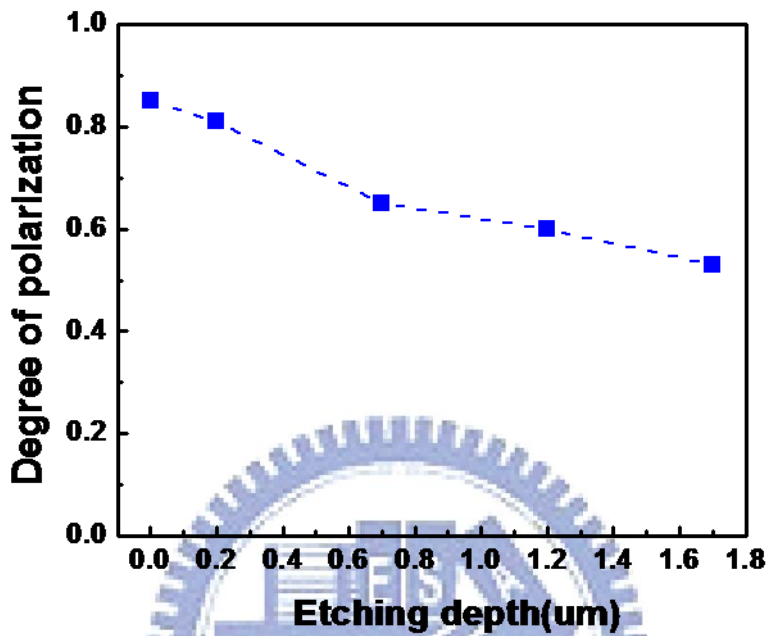
Fig. 4.4.3 The polarization ratio plotted as the function of nanorod etching depth at

300K.

	0um	0.2um	0.7um	1.2um	1.7um
DOP(@300k)	0.85	0.81	0.65	0.60	0.53
$\triangle E(meV)$	39	32	22	18	10

Table 4.4.1 The degree of polarization and peak energy shift with different nanorod
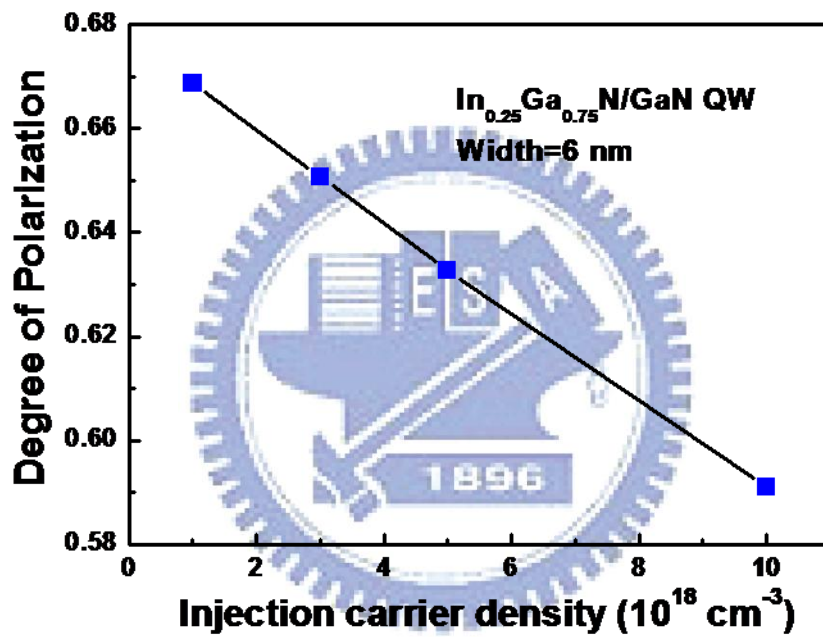
depth at 300K.

Fig 4.4.4 Simulated polarization degree with different injection carrier density of

$In_{0.25}Ga_{0.75}N$/GaN MQWs at 300K.
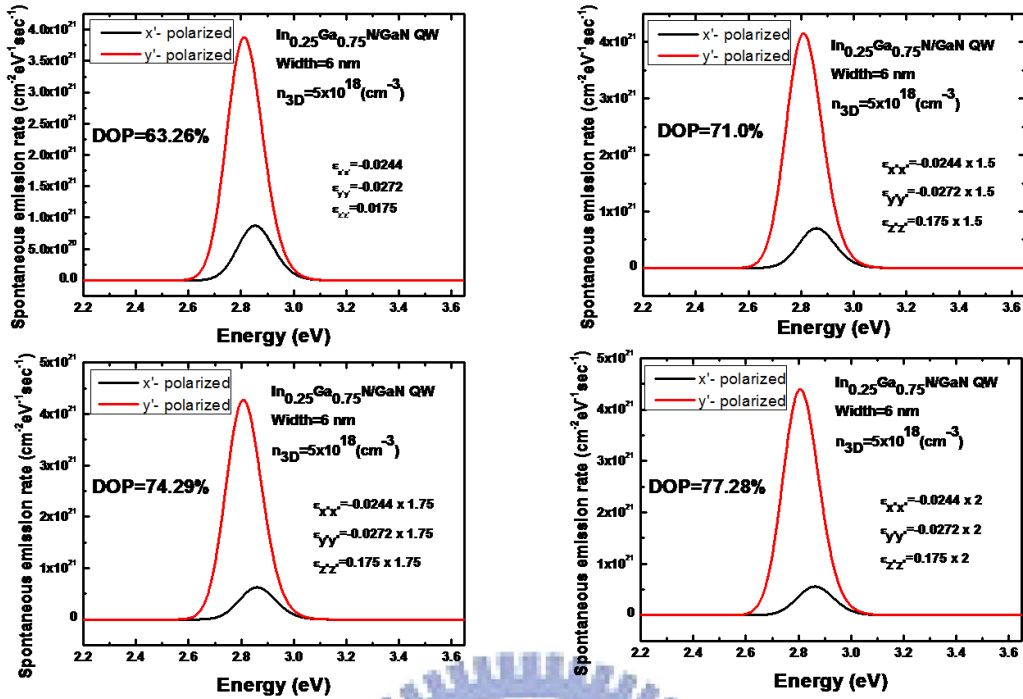
Fig 4.4.5 PL spectra simulated as a function of x'-polarized and y'-polarized of

In$_{0.25}$Ga$_{0.75}$N/GaN MQWs at 300K varied strain from 1a to 2a.
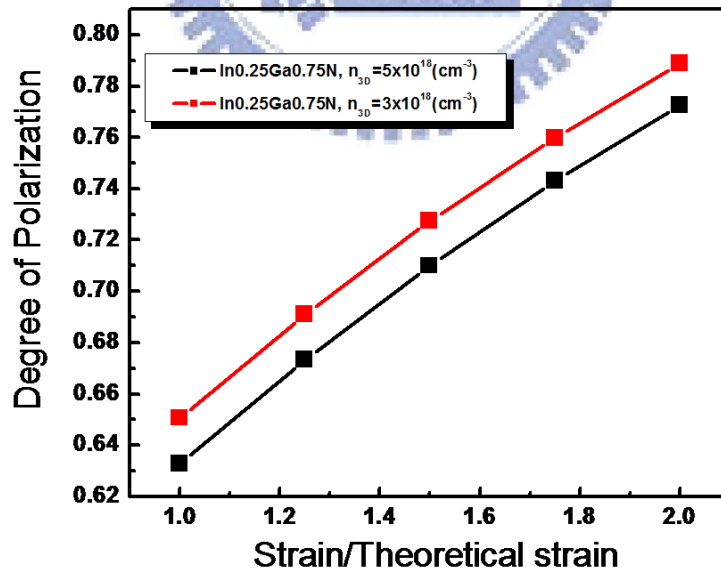
Fig 4.4.6 Simulated polarization degree with different strain of In$_{0.25}$Ga$_{0.75}$N/GaN with

different carrier density at 300K.
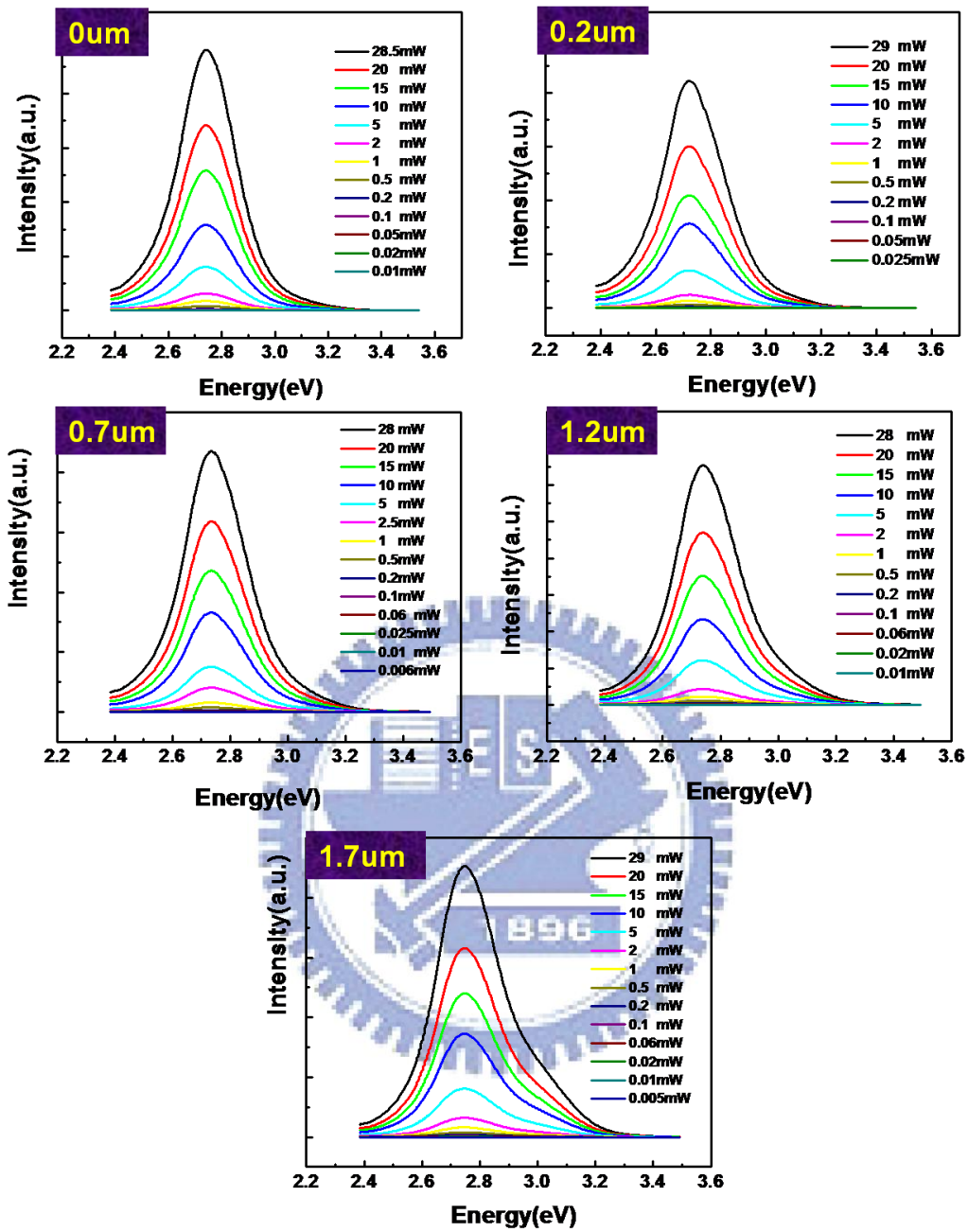
Fig. 4.5.1 PL spectra with different nanorod depth plotted as a function of excitation

power at 300K.
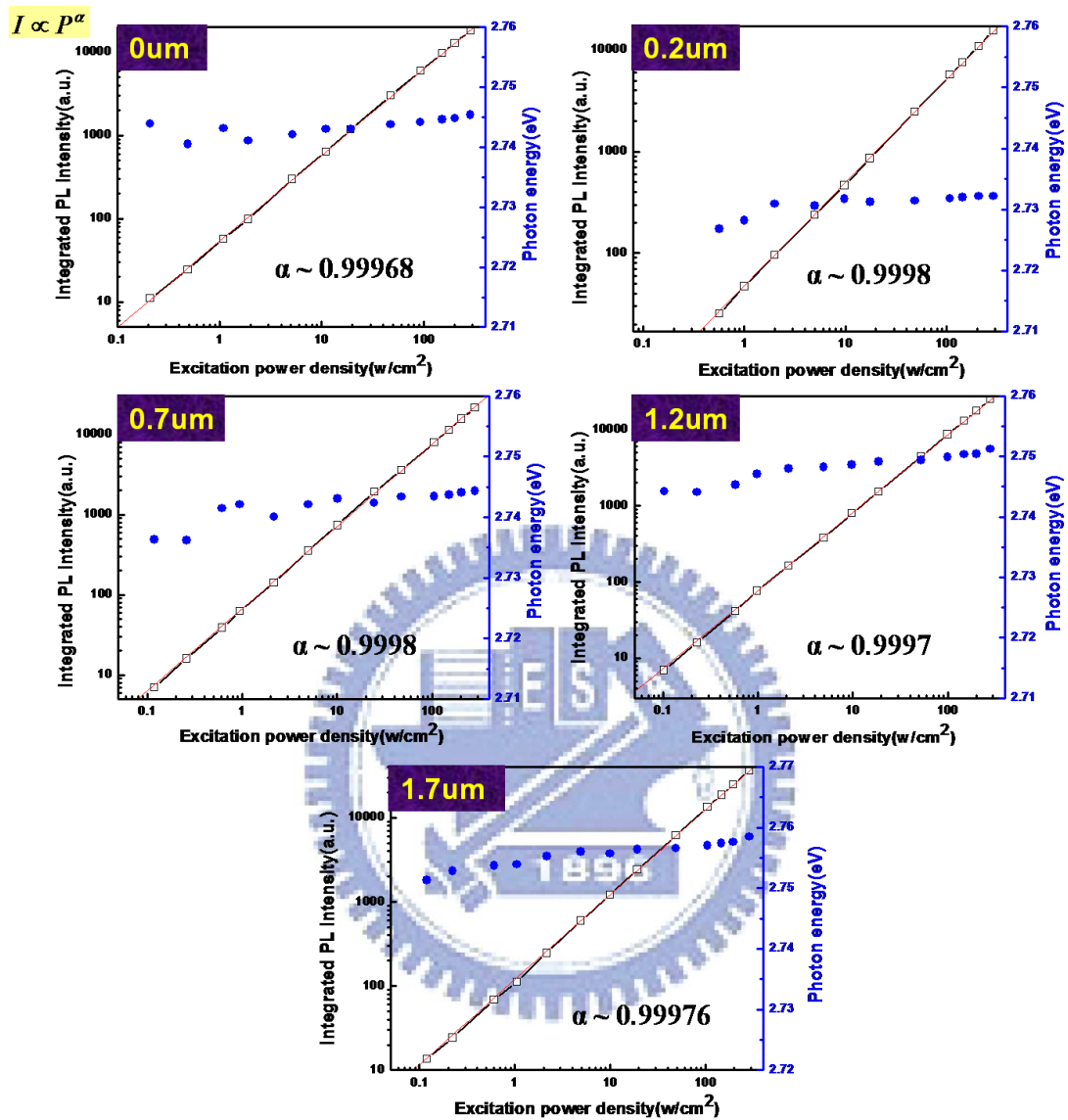
Fig4.5.2 Power-dependent PL fitting result for InGaN/GaN MQWs at 300K.
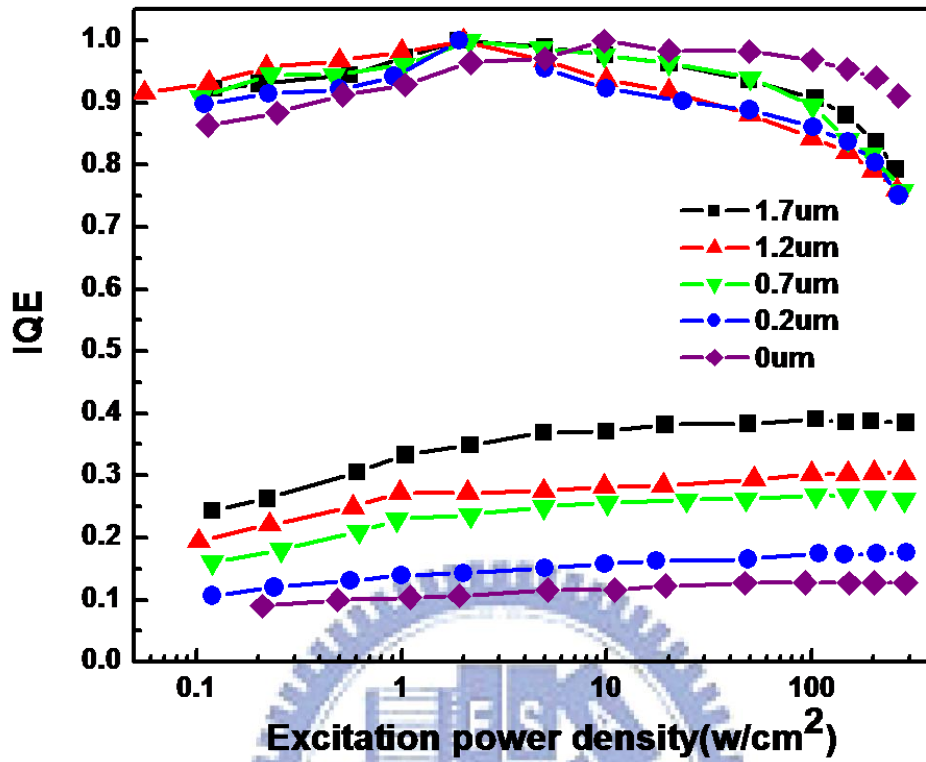
FIG. 4.6.1 Relative PL quantum efficiency as a function of excitation power density

for all samples measured at 300 and 20 K.
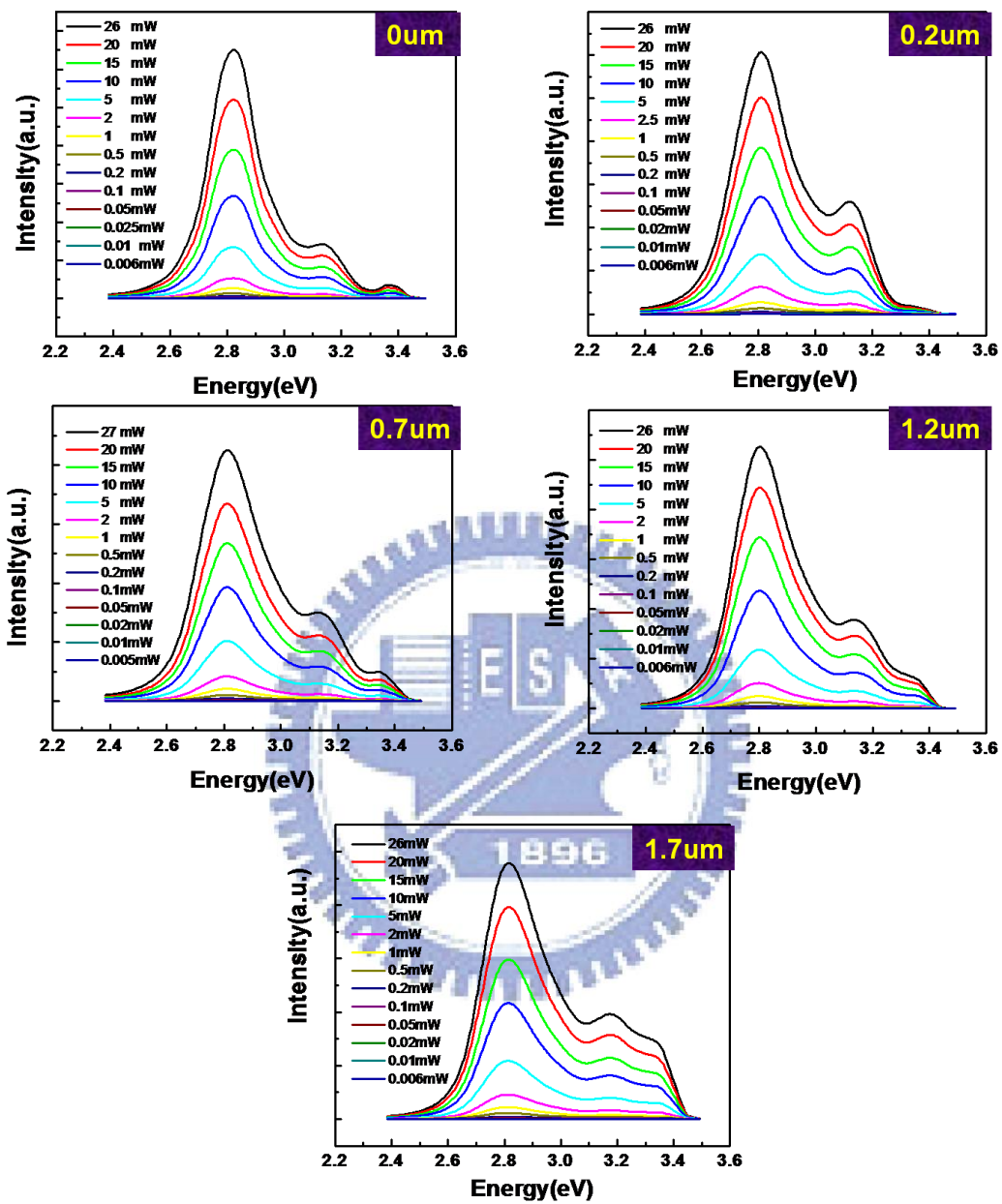
Fig. 4.6.2 PL spectra with different nanorod depth plotted as a function of excitation power at 20K.
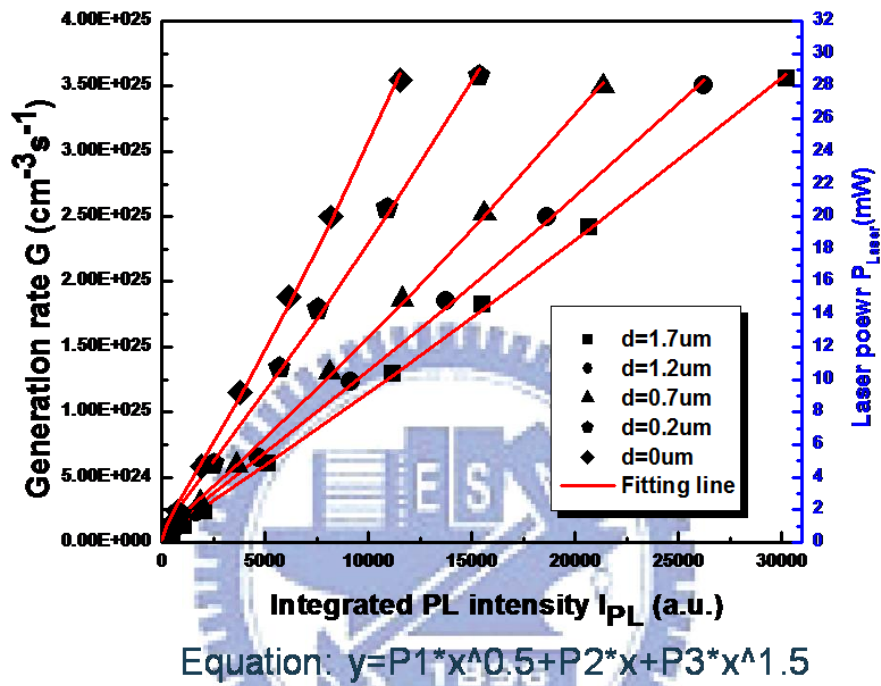
Fig. 4.6.3 (Color online) Generation rate *G* as a function of integrated PL intensity I_{PL}

of 1.7um and fitted curves obtained using Eq. (4.6.4).
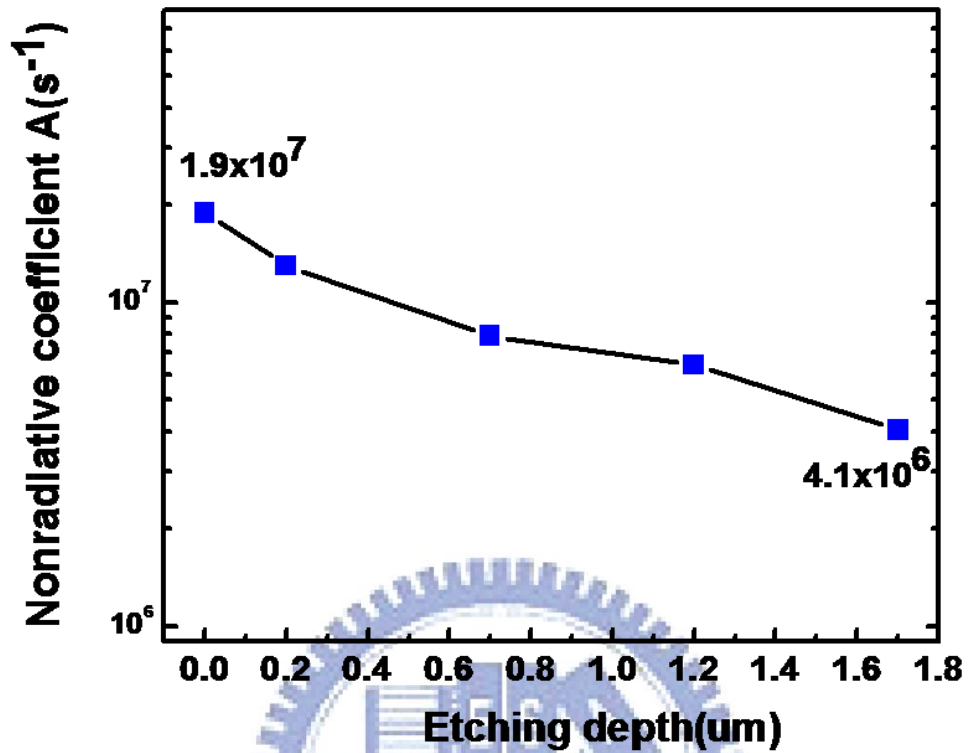
Fig. 4.6.4 (Color online) Nonradiative coefficient A as a function of nanorod etching

depth.

	0um	0.2um	0.7um	1.2um	1.7um
$A(s^{-1})$	1.9×10^7	1.3×10^7	7.9×10^6	6.42×10^6	4.1×10^6

Table 4.6.1 The value of nonradiative coefficient A with different nanorod depth at

300K.
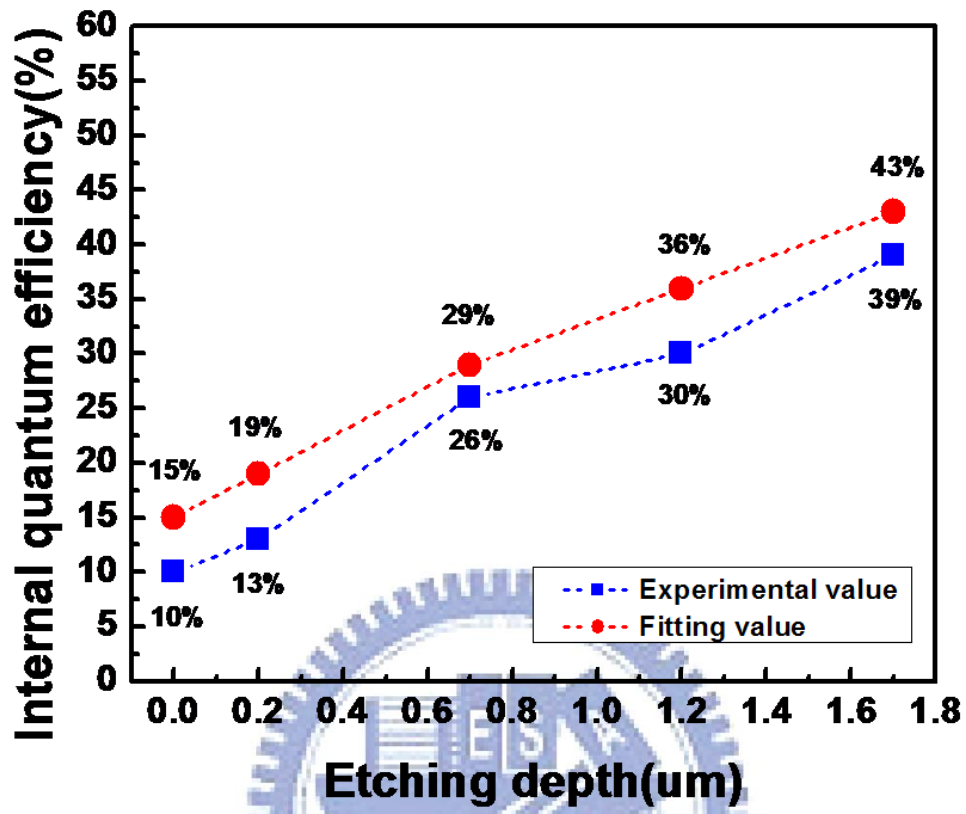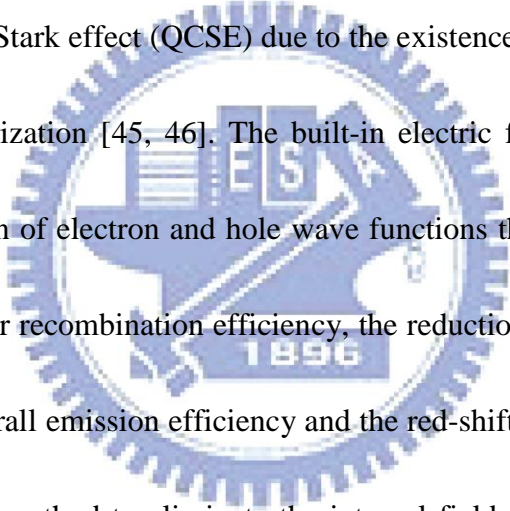
Fig. 4.6.5 (Color online) The internal quantum efficiency of fitting value compared with experimental value as a function of nanorod etching depth.

Chapter 5 Characteristics of emission polarization in *a*-plane nanorods embedded with InGaN/GaN MQWs

5.1 Introduction

GaN-based devices have attracted much attention for optoelectronic applications like laser diode and light emitting diode (LED) [44] due to their wide direct band gap with emission wavelength ranging from infrared to ultraviolet light. However, conventional *c*-plane multiple quantum well (MQW) structures suffer from the quantum confinement Stark effect (QCSE) due to the existence of strong piezoelectric and spontaneous polarization [45, 46]. The built-in electric fields along *c*-direction cause spatial separation of electron and hole wave functions that in turn gives rise to the restriction of carrier recombination efficiency, the reduction of oscillator strength, which reduced the overall emission efficiency and the red-shift of peak emission [47]. Recently, a promising method to eliminate the internal field is to grow InGaN/GaN MQWs on non-polar orientations such as {11-20} *a*-plane GaN on {10-12} *r*-plane sapphire and *a*-plane SiC, and {10-10} *m*-plane GaN on {100} LiAlO$_2$ substrates [48, 49]. In particular, due to the anisotropic in-plane compressive strain in nonpolar GaN-based materials, the original $|X \pm iY\rangle$-like valence-band states are broken into $|X\rangle$-like and $|Y\rangle$-like ones [50]. Therefore, an inherently polarized light will be emitted from InGaN/GaN MQWs grown on non-polar GaN, which is intriguing for

applications needing a polarized light source, such as liquid crystal display backlight

modules [51]. Theoretical studies predict that the polarization ratio increases as

indium composition increases [52]. However, it is well known that the low miscibility

of InN in GaN leads to a large fluctuations of indium or phase segregation within

InGaN layers [53, 54], which is believed to confine more carriers at localization

centers and then reduce the polarization ratio [55]. As a result, the polarization ratio

does not increase with the indium composition due to the enhancement of dotlike

In-rich regions [56]. In this paper, we reported a viable method by

nanorod-fabrication technique for improve the polarization ratio of a-plane

InGaN/GaN MQWs with higher indium composition. In addition, the optical

properties of a-plane GaN nanorod arrays with embedded InGaN/GaN MQWs on

r-plane sapphire were investigated to understand the origin for the variations of the

polarization ratio after nanorod-fabrication.
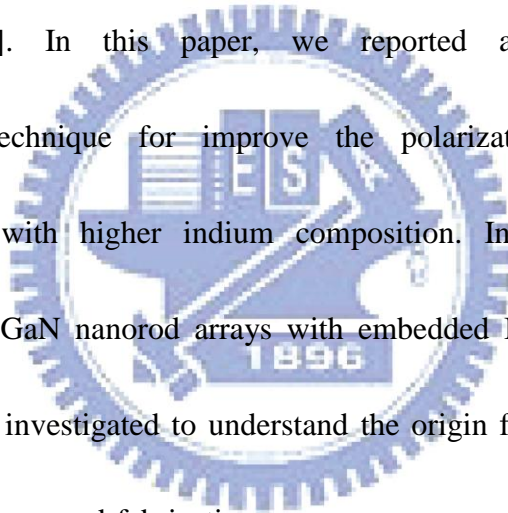
5.2 Experiment

Four a-plane $In_xGa_{1-x}N$/GaN MQWs with different indium compositions were

grown on r-plane sapphire with 0.2 offcut by metal organic chemical vapor deposition

(MOCVD) reactor. Trimethylgallium, trimethylindium, and ammonia were the

precursors used as sources of Ga, In, and N in whole epitaxial process. The a-plane

$In_xGa_{1-x}N$/GaN MQWs structures consisted 30-nm-thick AlN nucleation layer,

2-µm-thick bulk GaN, and 1-µm-thick *n*-type GaN, ten pairs MQWs with 18-nm-thick

GaN barrier and 4.5-nm-thick InGaN well and finally a 50-nm-thick GaN capping

layer. The detailed growth parameters were reported elsewhere [57]. The x-ray

diffraction analysis confirmed that the indium compositions of the quantum well are

around 0.09, 0.14, 0.24, and 0.30 for the four samples, respectively. The grown

a-plane LEDs were then subjected to the nanorod manufacturing process as shown in

Fig. 5.2.1 (a). First, a thin layer of Ni metal about 10 nm was deposited on the surface

by E-gun evaporator. The Ni-coated *a*-plane LED samples were subsequently

subjected to rapid temperature annealing (RTA) under flowing N_2 at 850 ^{o}C for 1 min

to form self-assembled Ni metal clusters. Then, the *a*-plane LED samples were etched

down to the *n*-type GaN layer by the ICP-RIE system (SAMCO ICP-RIE 101iPH)

operated at 13.56 MHz under a gas mixture of $Cl_2/Ar = 45/30$ sccm with 2 min of

etching time to form nanorods. The ICP source power, bias power and the chamber

pressure of the ICP-RIE system were set at 400/40 W. Finally, the samples were

dipped into a heated nitric acid solution (HNO_3) at 100 ^{o}C for 5 min to remove the

residual Ni nanomask. Figure 1(b) shows the birds-view (left) and cross-sectional

(right) FESEM image of the fabricated *a*-plane InGaN/GaN MQWs nanorods. The

dimension and density of the fabricated nanorods were estimated from the SEM

image to be around 250 nm and 1×10^9 cm^{-2}, respectively. The etching depth
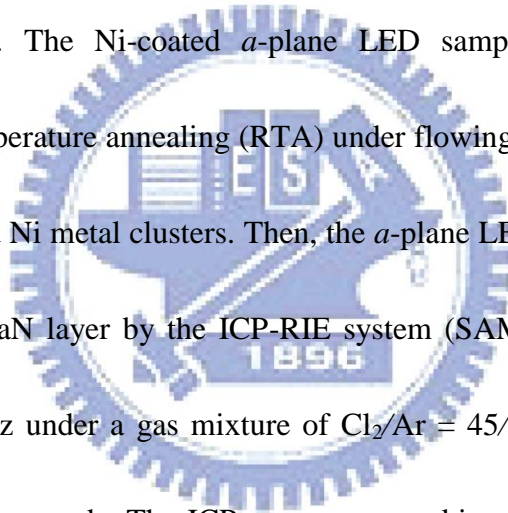
estimated from the image is about 0.6 µm.

For the polarization dependent photoluminescence (PL) measurements, the samples were excited by a 325 nm HeCd laser with an excitation power of 35 mW and the emitted luminescence light was collected using a polarizer in front of the spectrometer (Triax 320) with a charge-coupled device detector. As rotating the polarizer, we could collect the light with electrical field perpendicular ($E\perp c$) and parallel ($E//c$) to the c-axis, respectively. The focused spot size of the HeCd laser was estimated to be about 200 µm in diameter. In addition, temperature-dependent PL measurements were performed at temperatures ranging from 20 to 300 K.

5.3 Results and discussions

Figure 5.3.1 shows the integrated PL intensity of all samples after nanorod-fabrication at different polarization angles at room temperature. It can obviously be seen that the PL intensity for all four samples increases with increasing the polarization angle from 0° ($E//c$) to 90° ($E\perp c$), implying that polarized light has been emitted from the a-plane InGaN/GaN MQWs nanorods. Moreover, since the spectral broadening is too large (about 200 meV), observable peak shift can not be found between the emissions polarized to $E//c$ and to $E\perp c$. The polarization ratios (ρ) for all samples are calculated and summarized in Fig. 5.3.2., where ρ is defined as ($I_{\perp}$-$I_{//}$)/($I_{\perp}$+$I_{//}$) using the integrated PL intensity, I. At first glance, the polarization

ratio ρ still decreases as indium composition increases. Interestingly, it is found that, as compared with the as-grown samples, the values of ρ decreases slightly by 11% and 7% in the nanorod samples with x = 0.09 and 0.14, respectively, while increases significantly by 79% and 27% in the nanorod samples with x = 0.24 and 0.30, respectively. Previous structural and optical studies on the *c*-plane InGaN/GaN MQWs nanorods showed that the internal strain had been greatly reduced [58, 59]. Accordingly, the anisotropy strains in the *a*-plane InGaN/GaN MQWs nanorods should also be released. Once the strain is decreased, subband-energy separation should be smaller [60, 61], which will lead to the reduction of the polarization ratio. In addition, multiple scattering should occur after the nanorod formation, which also can reduce the polarization ratio. However, considering the anomalous enhancement of ρ in the higher indium composition samples after nanorod fabrication, one can expect that there must be other mechanisms accounting for this phenomenon. In the following, further optical studies and discussions are carried out.

The temperature-dependent PL spectra of all samples were measured between 20 and 300 K with 20 K interval. The results for the sample with indium composition of 0.09 are displayed in Fig. 5.3.3 as illustration. Similar to the as-grown samples, the spectra of nanorod samples exhibit lower-energy (P_L) and higher-energy (P_H) emission peaks in the low-temperature range, which are attributed to the emissions

from localized states and quantum wells, respectively. Nevertheless, it is noteworthy that both P_L and P_H peaks blueshift slightly after nanorod fabrication, and the P_H peak becomes dominant at low temperature. By fitting the PL spectrum with two Gaussian functions, the emission energies and intensities of the P_L and P_H peaks can be identified. Figure 5.3.4 shows the integrated intensity ratio of the P_L to P_H peaks (denoted as P_L/P_H) at 20 K for all samples before and after nanorod fabrication. An apparent reduction of P_L/P_H can be observed in all samples, and it is decreased by 35%, 60%, 65%, and 49% for nanorod samples with x = 0.09, 0.14, 0.24, and 0.3, respectively. This result suggests that the energy depth of localized states may have been reduced after nanorod fabrication. Thus more carriers would be confined in the quantized level of quantum well rather than in localized centers. In addition, the slight blueshift may also be attributed to these shallower localized states.

Furthermore, it has been studied that thermal quenching of PL intensity as temperature increased can be explained by the thermal emission of the carriers out of a confining potential with the activation energy. Therefore, it is expected that the shallower localized centers should have smaller activation energies. In order to verify that, the temperature dependence of PL intensity for all nanorod samples were fitted by Arrhenius equation:

$$I(T) = \frac{I_0}{1 + A\exp(\frac{-E_a}{k_B T}) + B\exp(\frac{-E_b}{k_B T})}.$$ (1)

where T is the temperature, I_T and I_0 are the integrated PL intensity for T and 0 K, A and B are constants, k_B is the Boltzmann constant, E_a is the activation energy for PL quenching, and E_b is generally associated to the free exciton binding energy [62]. The fitted activation energies E_a are listed in Table 5.3.1. Compared with the as-grown samples, the value of E_a is indeed smaller, as expected. Particularly, the largest variation of E_a (about 16 meV) appears in the sample with indium composition of 0.24, which is consisting with the greatest reduction of the integrated intensity ratio of the P_L to P_H peaks mentioned above.

Based on these results, the variations of the polarization ratio observed in our nanorod samples can be explained as follow. By fabricating the nanorod structures, multiple scattering along with strain relaxation and reduction of localized centers occur in all samples, which are believed to decrease and increase the polarization ratio of the emission, respectively. For the case of lower indium composition samples, the multiple scattering and strain-relaxation is considered to be much stronger. While as the indium composition is continuously increased, the polarization ratio enhancement effect by the reduction of localized centers becomes dominant. Therefore, slight reduction and evident enhancement of the polarization ratio are observed in our a-plane nanorod samples with lower and higher indium compositions, respectively. In

the future, more detailed study will be performed to quantify the strain-relaxation and understand the origin of the reduction of the energy depth of localized states.

5.4 Conclusion

In summary, *a*-plane GaN nanorod arrays with embedded $In_xGa_{1-x}N$/GaN MQWs (x=0.09, 0.14, 0.24, and 0.30) by self-assembled Ni clusters and RIE-ICP dry etching have been fabricated successfully and the optical properties were studied in this work. The polarization-dependent PL reveals that the polarization ratio decreases slightly by 11% and 7% in the nanorod samples with x= 0.09 and 0.14, respectively, while increases significantly by 79% and 27% in the nanorod samples with x= 0.24 and 0.30, respectively. Moreover, from temperature-dependent PL results, low- (P_L) and high-energy (P_H) PL peaks, related to localized states and quantum wells, respectively, can be observed at low temperature after nanorod fabrication, which is similar to the as-grown samples. However, the intensity-ratio of P_L and P_H decreases by 35%, 60%, 65%, and 49% for nanorod samples with increasing x from 0.09 to 0.30, respectively, indicating the reduction of localized states. This argument is verified from the smaller activation energies for PL quenching in the nanorod samples. In addition, multiple scattering along with strain relaxation is expected in these *a*-plane nanorod samples. Therefore, the variations of the polarization ratio mentioned above may be attributed to the competition between the polarization-ratio reduction and enhancement effect by

the multiple scattering along with strain relaxation and the reduction of localized

centers, respectively. These results suggest that the nanorod fabrication can be an

effective way to fabricate long-wavelength GaN-based LEDs with higher polarization

ratio.
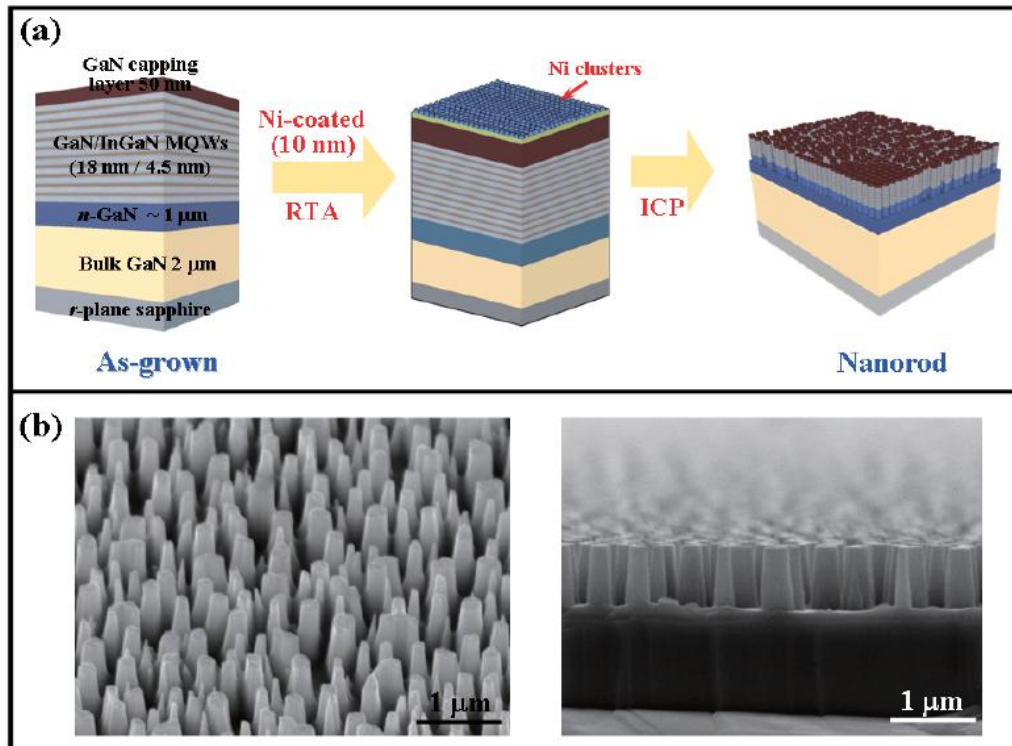
Fig. 5.2.1 (Color online) (a) The schematic of the *a*-plane InGaN/GaN MQWs nanorod fabrication process. (b) The birds-view (left) and cross-sectional (right) FESEM image of the fabricated *a*-plane InGaN/GaN MQW nanorods. The density, diameter and heights of the nanorods were and 1×10^9 cm^{-2}, 250 nm and 0.6 µm, respectively.
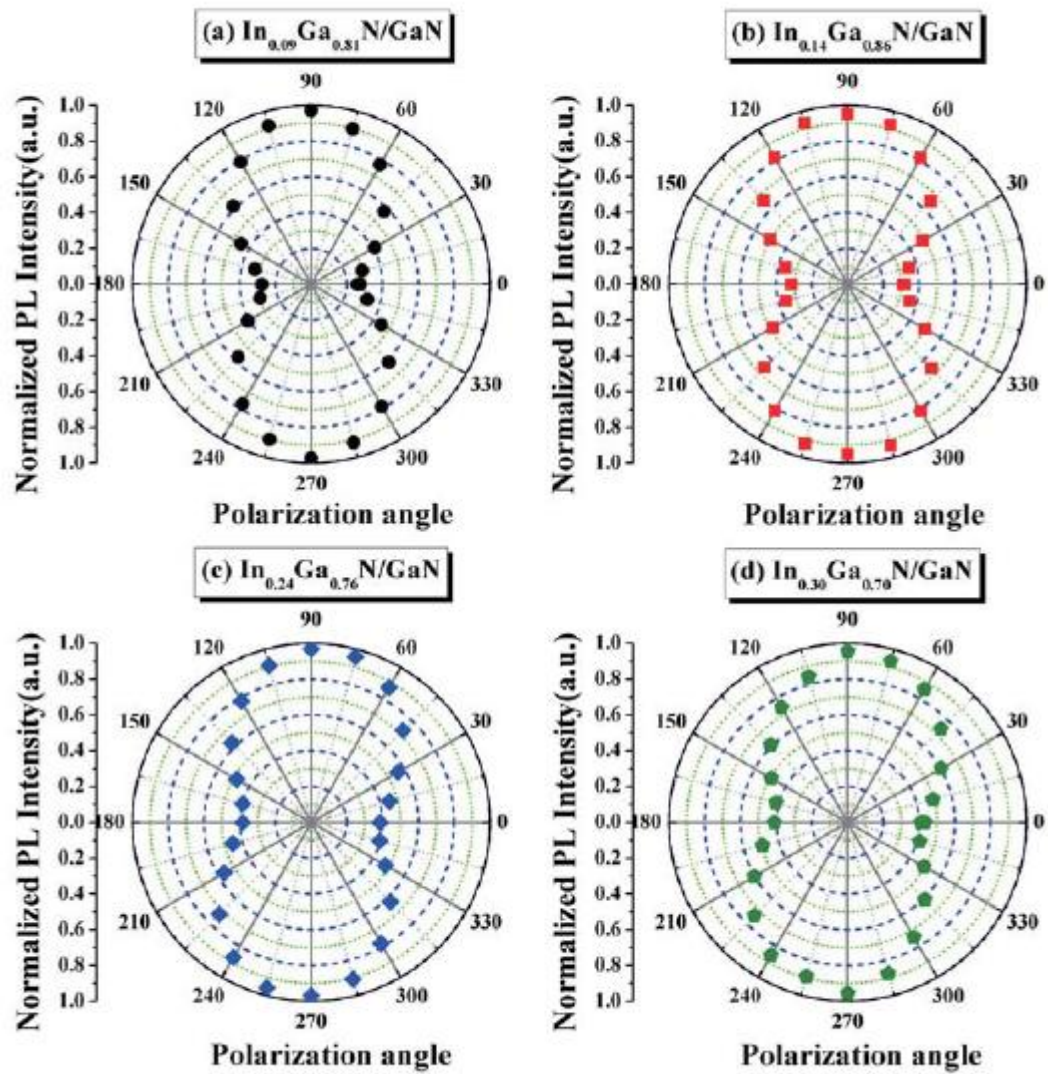
Fig. 5.3.1. (Color online) The integrated PL intensity of nanorod samples with indium

composition of (a) 0.09, (b) 0.14, (c) 0.24, and (d) 0.30 at different polarization angles

at room temperature.
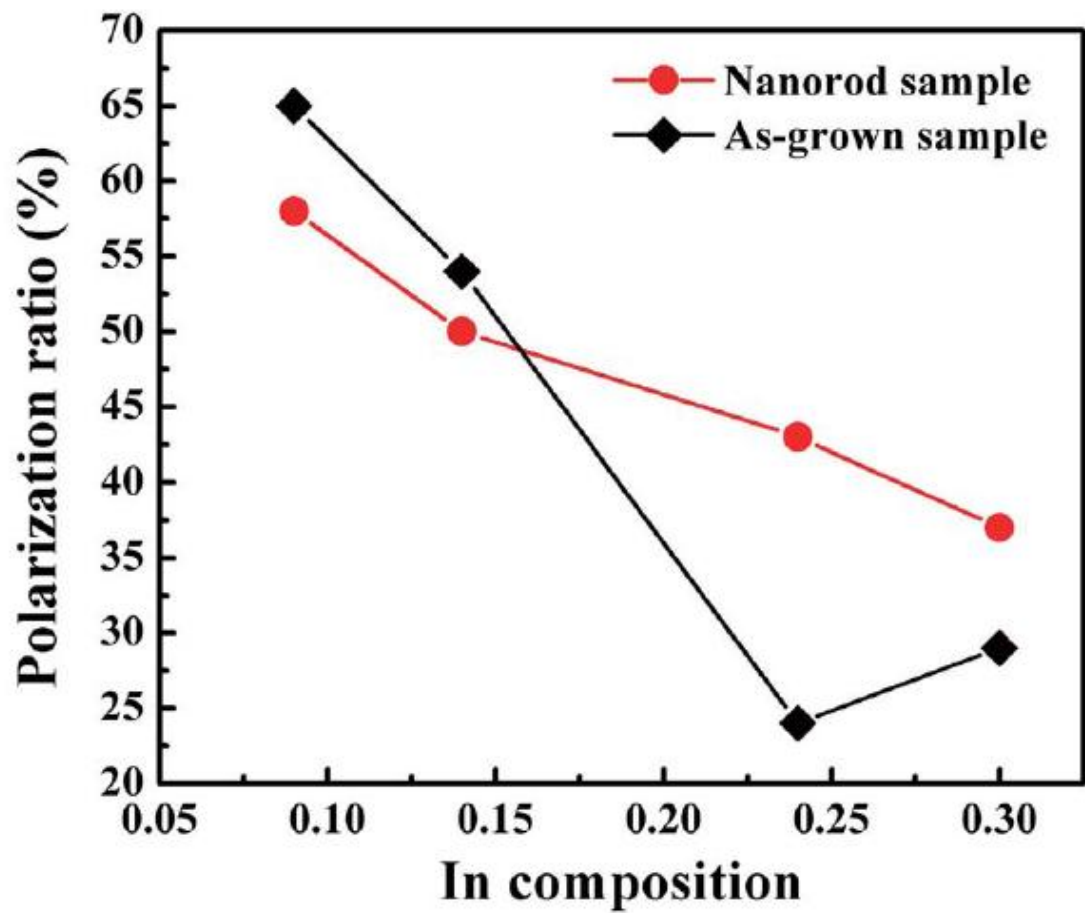
Fig. 5.3.2 (Color online) The polarization ratio plotted as the function of indium compositions for the as-grown and nanorod samples.
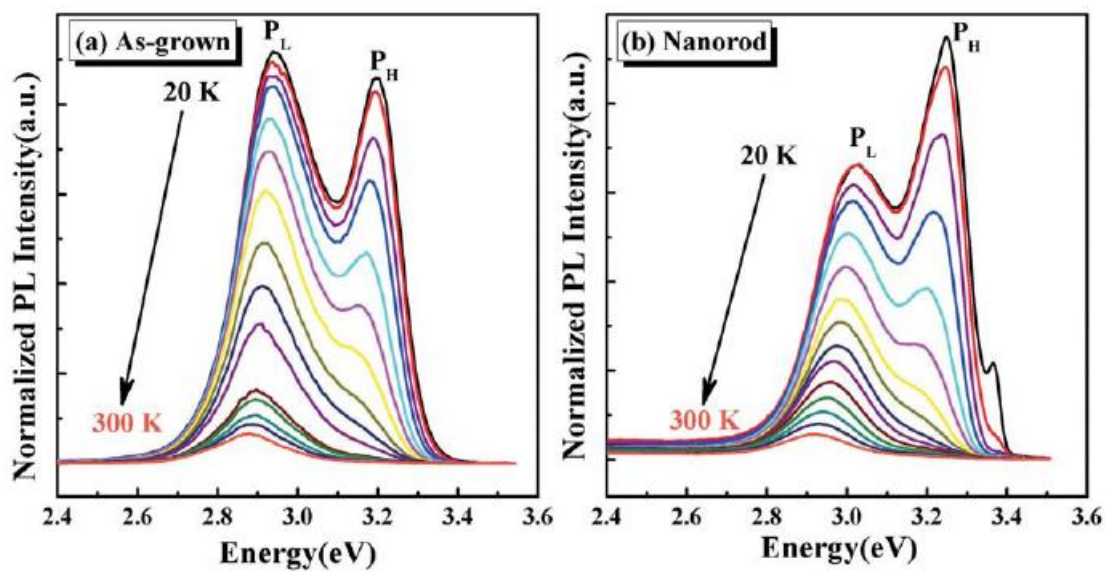
Fig. 5.3.3 (Color online) The temperature-dependent PL spectra for the (a) as-grown

and (b) nanorod samples with indium composition of 0.09. The temperature increases

from 20 K to 300 K with 20 K interval.
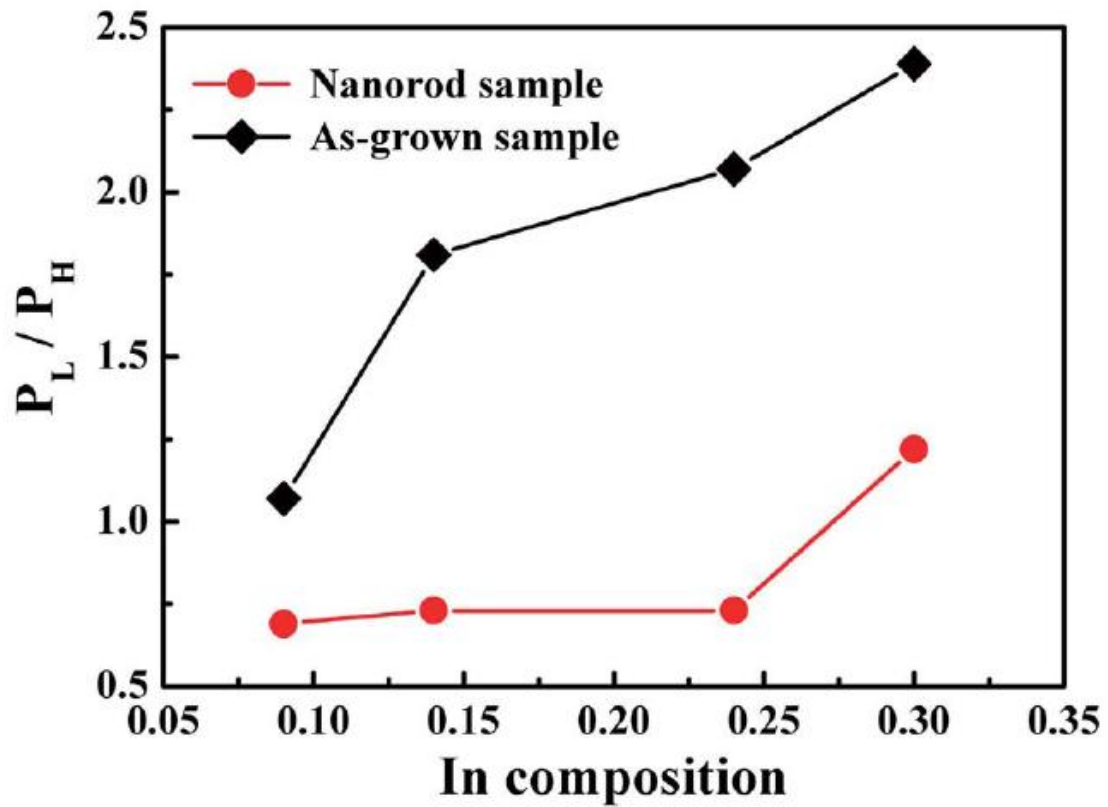
Fig. 5.3.5 (Color online) The integrated intensity ratio of the P_L to P_H peaks plotted as the function of indium compositions for the as-grown and nanorod samples measured at 20 K.

In composition	0.09	0.14	0.24	0.30
E_a (meV) As-grown	89	95	110	85
E_a (meV) Nanorod	83	91	94	78

Table 5.3.1 The fitted activation energy (E_a) for PL quenching for all as-grown and

nonorod samples.
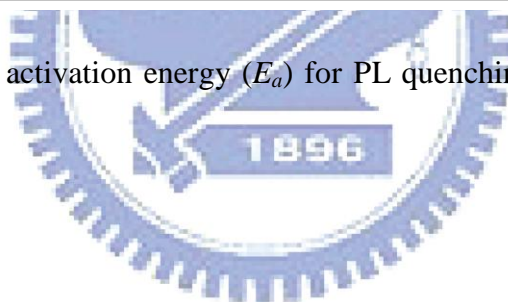
Chapter 6 Conclusion and future work

6.1 Conclusion

In this thesis, we investigated a-plane InGaN/GaN multiple quantum wells were grown on r-plane sapphire by metal organic chemical vapor deposition. The crystal quality of *a*-plane GaN films was improved by using epitaxial lateral overgrowth on a nanorod GaN template by AFM and TEM. Temperature dependent PL clearly showed the internal quantum efficiency increased with the depth of nanorod template and had an optimized value with 1.7um. As expected, the activation energy gradually increases and reaches the maximum value of 135 meV when nanorod depth is 1.7um. The trend of the activation energy is consistency with the internal quantum efficiency. The experiment results show that the polarization degree and peak energy shift (ΔE) was decreasing when the etching depth of nanorod was increasing. We could infer that strain is an important reason and prove our thoughts through simulation. No built-in electric field was observed in the power dependent PL measurement for all samples. The IQE of a-plane InGaN/GaN MQWs are approximately 39% (1.7um), 30% (1.2um), 26% (0.7um), 16% (0.2um), and 13%(0um) using PL with changing excitation power density at 300 and 20 K. The measured nonradiative recombination coefficient A varied from 1.9×10^7 to $4.1 \times 10^6 \text{ s}^{-1}$ as the etching depth increases from 0 to 1.7 um. From the TEM images, the average threading dislocation density was

estimated to be 1×10^9 cm^{-2}, which was about 1~2 orders magnitude lower than that in

as-grown GaN (3×10^{10} cm^{-2}). The threading-dislocation density significantly affects

the GaInN MQW efficiency, which supports the argument that threading dislocations

behave as nonradiative recombination centers. Therefore, the optical properties of

a-plane InGaN/GaN multiple quantum wells can be significantly improved by using

nanorod GaN template to reduce the defect densities.

6.2 Future work

In short, we have successfully grown the nonpolar InGaN/GaN MQWs by

MOCVD and measured the optical characteristics of all samples. More effort to

improve epitaxial crystal quality and more efforts on adjusting the epitaxial growth

conditions to reduce the defect densities would be the next step.
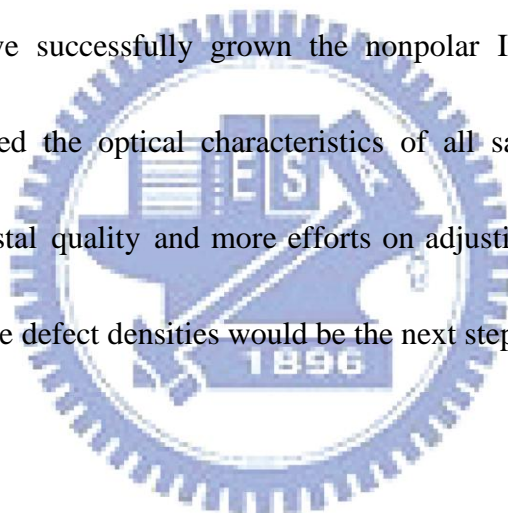
Reference

[1] F. Bernardini, V. Fiorentini, and D. Vanderbilt, Phys. Rev. B 56, R10024 (1997)

[2] T. Takeuchi, S. Sota, M. Katsuragawa, M. Komori, H. Takeuchi,H. Amano, and I. Akasaki, Jpn. J. Appl. Phys. 36, L382 (1997).

[3] P. Waltereit, O. Brandt, A. Trampert, H. T. Grahn, J. Menniger,M. Ramsteiner, M. Reiche, and K. H. Ploog, Nature 406, 865 (2000).

[4] Y. J. Sun, O. Brandt, S. Cronenberg, S. Dhar, H. T. Grahn, K. H. Ploog, P. Waltereit, and J. S. Speck, Phys. Rev. B 67, 041306 (2003).

[5] H. M. Ng, Appl. Phys. Lett. 80, 4369 (2002).

[6] H. M. Ng, A. Bell, F. A. Ponce, and S. N. G. Chu, Appl. Phys. Lett. 83, 653 (2003).

[7] M. D. Craven, P. Waltereit, J. S. Speck, and S. P. DenBaars, Appl. Phys. Lett. 84, 496 (2004).

[8] C. K. Sun, S. Keller, G. Gang, M. S. Minsky, J. E. Bowers, and S. P. DenBaars, Appl. Phys. Lett. 69, 1936 (1996).

[9] C. K. Sun, S. Keller, T. L. Chiu, G. Wang, M. S. Minsky, J. E. Bowers, and S. P.DenBaars, IEEE J. Quantum Electron. 3, 731 (1997).

[10] C. H. Chiu, S. Y. Kuo, M. H. Lo, C. C. Ke, T. C. Wang, Y. T. Lee, H. C. Kuo, T. C. Lu, and S. C. Wang, JOURNAL OF APPLIED PHYSICS 105, 063105 (2009)

[11] X. Ni, J. Lee, M. Wu, X. Li, R. Shimada, Ü . Ö zgür, A. A. Baski, H. Morkoç,T. Paskova, G. Mulholland, and K. R. Evans, APPLIED PHYSICS LETTERS 95, 101106 (2009)

[12] Y. R. Wu, C. H. Chiu, C. Y. Chang, P. C. Yu, and Hao-Chung Kuo, IEEE J. Quantum Electron. VOL. 15, NO. 4, JULY/AUGUST 2009

[13] A. Chakraborty, K. C. Kim, F. Wu, J. S. Speck, S. P. DenBaars, and U. K. Mishra, Appl. Phys. Lett. 89, 041903 (2006).

[14] B. A. Haskell, F. Wu, M. D. Craven, S. Matsuda, P. T. Fini, T. Fujii, K. Fujito, S. P. DenBaars, J. S. Speck, and S. Nakamura, Appl. Phys. Lett. 83, 644 (2003).

[15] C. Chen, J. Zhang, J. Yang, V. Adivarahan, S. Rai, S. Wu, H. Wang, W. Sun, M. Su, Z. Gong, E. Kuokstis, M. Gaevski, and M. A. Khan, Jpn. J. Appl. Phys., Part 2 42, L818 (2003).

[16] B. Imer, F. Wu, S. P. DenBaars, and J. S. Speck, Appl. Phys. Lett. 88, 061908 (2006).

[17] S. C. Ling, C. L. Chao, J. R. Chen, P. C. Liu, T. S. Ko, T. C. Lu, H. C. Kuo, S. C. Wang, S. J. Cheng, and J. D. Tsay, APPLIED PHYSICS LETTERS 94, 251912 (2009)

[18] Leroux M, Grandjean N, Laugt M, Massies J, Gil B, Lefebvre P and Bigenwald P 1998 Phys. Rev. B 58 R13371

[19] S. Chichibu, T. Azuhata, T. Sota, and S. Nakamura, Appl. Phys. Lett. 69, 4188

(1996)

[20] I. Ho and G. B. Stringfellow, Appl. Phys. Lett. 69, 2701 (1996)

[21] P. Waltereit et al., J. Cryst. Growth 437, 227 (2001).

[22] S. F. Chichibu, T. Onuma, T. Aoyama, K. Nakajima, P. Ahmet, T. Chikyow, T.

Sota, S. P. DenBaars, S. Nakamura, T. Kitamura, Y. Ishida and H. Okumura : J.

Vac. Sci. & Technol. B 21, 1856 (2003)

[23] M. D. Craven, S. H. Lim, F. Wu, J. S. Speck, and S. P. DenBaars, Appl. Phys

Lett. 65 81, 469 (2002)

[24] S. Ghosh, P. Waltereit, O. Brandt, H. T. Grahn, and K. H. Ploog, Appl. Phys Lett.

80, 413 (2002)

[25] B. Rau, P. Waltereit, O. Brandt, M. Ramsteiner, K. H. Ploog, J. Puls, and F.

Henneberger, Appl. Phys Lett. 77, 3343 (2000)

[26] K. Domen, K. Horino, A. Kuramata, and T. Tanahashi, Appl. Phys Lett. 71, 1996

(1997)

[27] J. Shakya, K. Knabe, K. H. Kim, J. Li, J. Y. Lin, and H. X. Jiang, Appl. Phys

Lett. 86, 091907 (2005)

[28] S. Nakamura and G. Fasol, The Blue Laser Diode (Springer, Berlin, 1997).

[29] M. D. Craven, S. H. Lim, F. Wu, J. S. Speck, and S. P. DenBaars, Appl.Phys.

Lett. 81, 469 (2002).

[30] R. W. Martin, P. G. Middleton, K. P. O'Donnell, and W. Van Der Stricht, Appl. Phys. Lett. 74, 263 (1999).

[31] Y.-h. Wu, K. Arai, and T. Yao, Phys. Rev. B 53, R10485 (1996).

[32] J. S. Hwang, A. Gokarna, and Y,-H. Choa, J. Appl. Phys. 102, 013508 (2007).

[33] Y. H. Cho, G. H. Gainer, A. J. Fischer, J. J. Song, S. Keller, U. K. Mishra, and S. P. DenBaars, Appl. Phys. Lett. 73, 1370 (1998).

[34] A. Yasan, R. McClintock, K. Mayes, D. H. Kim, P. Kung, and M. Razeghi, Appl. Phys. Lett. 83, 4083 (2003).

[35] M. Leroux, N. Grandjean, B. Beaumont, G. Nataf, F. Semond, J. Massies, and P. Gibart, J. Appl. Phys. 86, 3721 (1999).

[36] E. Kuokstis, C. Q. Chen, M. E. Gaevski, W. H. Sun, J. W. Yang, G. Simin, and M. A. Khan, Appl. Phys. Lett. 81, 4130 (2002).

[37] T. Takeuchi, S. Sota, M. Katsuragawa, M. Komori, H. Takeuchi, H. Amano, and I. Akasaki, Jpn. J. Appl. Phys., Part 2 36, L382 (1997).

[38] S. Watanabe and N. Yamada, Appl. Phys. Lett. Vol. 83, No. 24, 15 December (2003)

[39] H. Kudo, K. Murakami, R. Zheng, Y. Yamada, T. Taguchi, K. Tadatomo, H. Okagawa, Y. Ohuchi, T. Tsunekawa, Y. Imai, and M. Kato, Jpn. J. Appl. Phys.

41, 2484 (2002).

[40] Q. Dai, M. F. Schubert, M. H. Kim, J. K. Kim, E. F. Schubert, D. D. Koleske, M.

H. Crawford, S. R. Lee, A. J. Fischer, G. Thaler, and M. A. Banas, Appl. Phys.

Lett. 94, 111109 (2009).

[41] X. Li, X. Ni, J. Lee, M. Wu, Ü. Özgür, H. Morkoç, T. Paskova, G. Mulholland,

and K. R. Evans, APPLIED PHYSICS LETTERS 95, 121107 (2009)

[42] J. S. Speck and S. J. Rosner, Physica B 273, 24 (1999).

[43] P. G. Eliseev, M. Osin'ski, H. Li, and I. V. Akimova, Appl. Phys. Lett. 75, 3838

(1999).

[44] S. Nakamura, M. Senoh, S. Nagahama, N. Iwasa, T. Yamada , T. Matsushita, H.

Kiyoku, and Y. Sugimoto, Japan. J. Appl.Phys., **35**, L74 (1996).

[45] W. H. Sun, J. W. Yang, C. Q. Chen, J. P. Zhang, M. E. Gaevski, E. Kuokstis, V.

Adivarahan, H. M. Wang, Z. Gong, M. Su, and M. A. Kahn, Appl. Phys. Lett., **83**,

2599 (2003).

[46] B. A. Haskell, F. Wu, M. D. Craven, S. Matsuda, P. T. Fini, T. Fujii, K. Fujito, S.

P. DenBaars, J. S. Speck, and S. Nakamura, Appl. Phys. Lett., **83**, 644 (2003).

[47] A. Chakraborty, S. Keller, C. Meier, B.A. Haskell, S. Keller, P. Waltereit, S. P.

DenBaars, S. Nakamura, J. S. Speck, and U. K. Mishra, Appl. Phys. Lett., **86**,

031901 (2005).

[48] A. Chitnis, C. Chen, V. Adivarahan, M. Shatalov, E. Kuokstic, V. Mandavilli, J. Yang, and M. A. Khan, Appl. Phys. Lett., **84**, 3663 (2004).

[49] P. Waltereit, O. Brandt, A. Trampert, H. T. Grahn, J. Menniger, M. Ramsteiner, M. Reiche, and K. H. Ploog, Nature, **406**, 865 (2000).

[50] S. Ghosh, P. Waltereit, O. Brandt, H. T. Grahn, and K. H. Ploog, Phys. Rev. B, **65**, 075202 (2002).

[51] H. Masui, H. Yamada, K.Iso, J. S. Speck, S. Nakamura, and S. P. DenBaars, J. Soc. Inf. Disp., **16**, 571 (2008).

[52] H - H. Huang, and Y - R. Wu, J. Appl. Phys., **106**, 023106 (2009).

[53] M. D. McCluskey, L. T. Romano, B. S. Krusor, D. P. Bour, N. M. Johnson, and S. Brennan, Appl. Phys. Lett., **72**, 1730 (1998).

[54] N. A. EI-Masry, E. L. Piner, S. X. Liu, and S. M. Bediar, Appl. Phys. Lett., **72**, 5 (1998).

[55] T. Koyama, T. Onuma, H. Masui, A. Chakraborty, B. A. Haskell, S. Keller, U. K. Mishra, J. S. Speck, S. Nakamura, S. P. DenBaars, and T. Sota, Appl. Phys. Lett., **89**, 091906 (2006).

[56] C. H. Chiu, S. Y. Kuo, M. H. Lo, C. C. Ke, T. C. Wang, Y. T. Lee, H. C. Kuo, T. C. Lu, and S. C. Wang, J. Appl. Phys., **105**, 063105 (2009).

[57] T.S. Ko, T. C. Wang, R. C. Gao, H. G. Chen, G. S. Huang, T. C. Lu, H. C. Kuo,

and S. C. Wang, J. Cryst. Growth, **300**, 308 (2007).

[58] C. H. Chiu, M. H. Lo, C. F. Lai, T. C. Lu. H. W. Huang, Y. A. Chang, T. H. Hsueh, C. C. Yu, H. C. Kuo, S. C. Wang, C. F. Lin, and Y. K. Kuo, Nanotechnology, **18,** 335706 (2007).

[59] Y. R. Wu, C. H. Chiu, C. Y. Chang, P. C. Yu, and H. C. Kuo, IEEE J. Sel. Topic Quantum Electron., **15,** 1226 (2009).

[60] B. Liu, R. Zhang, Z. L. Xie, J. Y. Kong, J. Yao, Q. J. Liu, Z. Zhang, D. Y. Fu, X. Q. Xiu, P. Chen, P. Han, Y. Shi, Y. D. Zheng, S. M. Zhou, and G. Edwards, Appl. Phys. Lett., **92**, 261906 (2008).

[61] D. Fu, R. Zhang, B. Wang, Z. Zhang, B. Liu, Z. Xie, X. Q. Xiu, H. Lu, Y. D. Zheng, and G. Edwards, J. Appl. Phys., **106**, 023714 (2009).

[62] M. Leroux, N. Grandjean, B. Beaumont, G. Nataf, F. Semond, J. Massies, and P. Gibart, J. Appl. Phys., **86**, 3721 (1999).